This is a repository copy of *Advanced Γ method for small-scale vortex detection in the solar atmosphere*.

White Rose Research Online URL for this paper:
https://eprints.whiterose.ac.uk/202179/

Version: Published Version

Advanced Γ Method for Small-scale Vortex Detection in the Solar Atmosphere

Yuyang Yuan[1] , Suzana de Souza e Almeida Silva[2] , Viktor Fedun[2] , Irina N. Kitiashvili[3] , and Gary Verth[1]
[1] Plasma Dynamics Group, School of Mathematics and Statistics, University of Sheffield, Hicks Building, Hounsfield Road, Sheffield, S3 7RH, UK
[2] Plasma Dynamics Group, Department of Automatic Control and Systems Engineering, The University of Sheffield, Mappin Street, Sheffield, S1 3JD, UK
[3] NASA Ames Research Center, Moffett Field, MS 258-5, Mountain View, CA 94035, USA
Received 2022 October 24; revised 2023 March 13; accepted 2023 March 26; published 2023 August 1

Abstract

Ubiquitous vortical structures are considered to act as a natural source of various solar plasma phenomena, for example, a wide range of magnetohydrodynamic waves and jet excitations. This work aims to develop an advanced vortex detection algorithm based on the Γ method and using a separable convolution kernel technique. This method is applied to detect and analyze the photospheric vortices in 3D realistic magnetoconvection numerical and observational data. We present the advanced Γ method (AGM), and our results indicate that the AGM performs with better accuracy in comparison with the original Γ method. The AGM allows us to identify small- and large-scale vortices with no vortex interposition and without requiring the changing of the threshold. In this way, the nondetection issue is mostly prevented. It was found that the Γ method failed to identify the large and longer-lived vortices, which were detected by the AGM. The size of the detected vortical structures tends to vary over time, with most vortices shrinking toward their end. The vorticity at the center is also not constant, presenting a sharp decay as the vortex ceases to exist. Due to its capability of identifying vortices with minimum nondetection, the vortex properties—such as lifetime, geometry, and dynamics—are better captured by the AGM than by the Γ method. In this era of new high-resolution observation, the AGM can be used as a precise technique for identifying and performing statistical analysis of solar atmospheric vortices.

Unified Astronomy Thesaurus concepts: Solar atmosphere (1477); Solar atmospheric motions (1478)

1. Introduction

In the solar atmosphere, vortical plasma motions are an important part of its dynamics. They may be responsible for magnetohydrodynamic (MHD) wave excitation (Schuessler 1984; Attie et al. 2009; Fedun et al. 2011; Kitiashvili et al. 2011; Yadav et al. 2022) and the formation of plasma jets (Kitiashvili et al. 2013; Iijima & Yokoyama 2017; Snow et al. 2018; Skirvin et al. 2023) and act as a channel for energy transfer to the solar corona (Shelyag et al. 2012; Wedemeyer-Böhm et al. 2012; Yadav et al. 2021). To understand the mechanism of vortex formation and its role in the plasma processes mentioned above, the precise automated identification of a vortex structure is essential (Tziotziou et al. 2023). However, the identification of vortices in solar numerical and observational data is still a challenge, as there is no universal definition for vortex motion (e.g., Günther & Theisel 2018). Numerous identification approaches have been developed based on distinct definitions of what constitutes a vortex. Initially, investigations of vortical structures in the solar atmosphere were based on visual inspection of the velocity field (Nordlund 1985; Brandt et al. 1988; Attie et al. 2009; Bonet et al. 2010) or detected motion of magnetic elements (Bonet et al. 2008; Balmaceda et al. 2010). Automated methodologies for vortex identification in solar physics were only introduced in the last decade by Moll et al. (2011), when they detected photospheric vortices using the swirling strength (Zhou et al. 1999), which was also used in posterior studies by Yadav et al. (2020) and Canivete Cuissa & Steiner (2020). For a velocity field U, the swirling strength is based on the velocity

field tensor, $D = \nabla U$, and it determines the vortex as a region where the eigenvalues of D are complex. Kato & Wedemeyer (2017) introduced a similar criterion, the vorticity strength, where a vortex region is identified as a local area where the eigenvalues of D are imaginary. The problem with such methods is that they provide a swirling region of the velocity field without giving proper information of the vortex boundary and centers. Therefore, the analysis of plasma properties and dynamics across the vortex using such techniques is not precise.

The first study on the identification of a well-defined boundary and center for vortical structures in the solar photosphere was presented by Giagkiozis et al. (2018), who analyzed a quiet-Sun region by applying the Γ method (Graftieaux et al. 2001), which is based on local analysis of the velocity vector field, to the CRisp Imaging Spectro-Polarimeter (CRISP; Scharmer 2006; Scharmer et al. 2008). Other identification methods that provide the vortex center and boundary are the Lagrangian averaged vorticity deviation (LAVD) and its Eulerian version, instantaneous vorticity deviation (IVD), both defined by Haller et al. (2016). Those methods are based on vorticity and have been used to analyze vortices from observations (Silva et al. 2018; Chian et al. 2019, 2020) and simulations (Silva et al. 2020, 2021; Aljohani et al. 2022). Silva et al. (2018) compared the performance of three vortex identification methods. It was found that LAVD and vorticity strength are prone to false identifications without an additional requirement, whereas the Γ method may not detect or provide false detections of some vortex structures. Researchers addressed these issues by introducing a novel criterion "d" when applying the LAVD and vorticity strength. This criterion can also be combined with other detection methods to address the false detection in shear flow.

All the vortex methods briefly described above have their advantages, depending on the goal of the analysis to be performed. Günther & Theisel (2018) have summarized existing methods according to the reference-frame invariance. Noninvariant detection techniques, such as visual inspection of the velocity field, refer to those methods that are suitable to the situation only when investigating the steady flow or the flow appears to be steady when choosing the right reference frame. Besides those noninvariant techniques, the remaining vortex detection methods are invariant under specific types of reference-frame motion. The vortex identification technique vorticity/swirling strength and Γ method are Galilean-invariant. Objective methods like LAVD or IVD are invariant when the reference frame is undergoing constant rotation and translation motion (see, e.g., Günther & Theisel 2018). Another approach, that is, the morphological method, which is applicable to the detection of chromospheric vortical motions, was recently proposed by Dakanalis et al. (2021, 2022).

Applying different vortex detection methods to solar data, both observational and simulation, has provided important information on vortex properties. By visual inspection of magnetic bright points from *G*-band images obtained from the Swedish Solar Telescope, Bonet et al. (2008) found several plasma vortices with sizes ranging from 0.5 to 2 Mm and lifetimes between 5 and 15 minutes in regions near the downdrafts of intergranular lanes. However, using magnetic bright points to identify vortices is not precise, as it can also overestimate the size of vortical structures and may interpret two close-by consecutive vortices as the same structure. The study by Giagkiozis et al. (2018) found an average lifetime of 17 s for intensity vortices detected by the Γ method, and their statistical analysis also indicated the vortices have a diameter of around 568 km. In MURaM simulations, vortex identification with IVD indicated a longer average lifetime, around 84.7 s, and a diameter approximately seven times smaller. At supergranular scales, vortices have been detected by visual inspection (Attie et al. 2009), cork tracking (Requerey et al. 2018), and LAVD (Chian et al. 2019, 2020). While visual inspection provided sizes around 15–20 Mm, the LAVD identified vortices with a smaller range, 5–10 Mm. In all the supergranular analyses, there are persistent vortical structures that last for a couple of hours.

In this paper, we introduce the advanced Γ method (AGM), which is based on the original Γ method proposed by Graftieaux et al. (2001). By comparing the Γ method and the AGM, we show that our technique reduces the influence of threshold choices. The AGM is applied to detect a solar vortex in a simulated solar surface obtained by StellarBox (a 3D radiative MHD code). We investigate the lifetimes, sizes, and dynamics of the velocity field components of the detected vortices. The new detection method is also applied to CRISP observational data and compared with the numerical data results.

The paper is structured as follows. First, in Section 2, we describe the AGM technique and the algorithm construction. Then, in Section 3, we provide detection results and statistical analysis and compare the performance of the AGM with the Γ method. Last, the discussion and conclusions are given in Section 4.
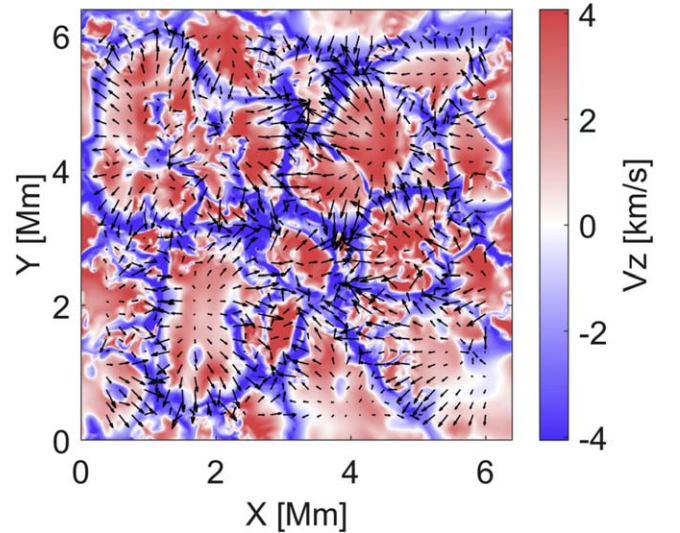

Figure 1. A snapshot of the magnetoconvection simulation at $t = 5$ s, displaying the simulated solar surface colored by the vertical velocity field. The black arrows show the direction of the horizontal velocity field.

2. Vortex Identification

2.1. Description of Simulation Data

For the numerical modeling, we use a 3D radiative MHD code, StellarBox (see, e.g., Kitiashvili et al. 2012; Wray et al. 2015), developed for realistic simulations of the upper convective zone and lower atmosphere. The size of the simulation area is 6.4×6.4 Mm, and it initially had an imposed uniform vertical magnetic field around 10 G. The simulation has a cadence of 5 s and the analyzed data have a total duration of 625 s. For our investigations, we used the horizontal velocity field from the simulated solar surface with a resolution of 12.5 km in the *x*- and *y*-directions. An example of a simulated horizontal velocity field snapshot is shown in Figure 1.

2.2. Vortex Identification by the Γ Method

For vortex identification, that is, its center and boundary, Graftieaux et al. (2001) introduced two dimensionless scalar functions, Γ_1 and Γ_2, respectively. It was shown that these two functions are able to detect large-scale vortices in turbulent flows.

The discrete version of Γ_1 at a given point *P* (within the numerical domain) can be represented as

$$\Gamma_1(P) = \frac{1}{N}\sum_S \frac{(\boldsymbol{PM} \times \boldsymbol{U_M}) \cdot \boldsymbol{z}}{\|\boldsymbol{PM}\| \cdot \|\boldsymbol{U_M}\|} = \frac{1}{N}\sin(\theta_M), \qquad (1)$$

where *N* is the number of discretely sampled velocity field points of a 2D area *S* centered on *P*. Point *M* lies within *S*, and $\boldsymbol{PM}$ denotes the displacement vector from point *P* to *M*. The variable $\boldsymbol{U_M}$ denotes the velocity vectors at point *M*, and $\boldsymbol{z}$ is a unit vector normal to the horizontal plane. The $\|\cdot\|$ notation represents magnitude.

The Γ_1 function defined in Equation (1) provides a scalar field that quantifies the topology of the flow in the neighboring region of *P*. At the vortex center, $|\Gamma_1|$, the cross-product value $\boldsymbol{PM} \times \boldsymbol{U_M}$ has a maximum, leading to the highest value of $|\Gamma_1|$. The sign of the Γ_1 value at the vortex center indicates the direction of the vortex rotation; that is, negative indicates that

the rotation is clockwise rotation and positive means it is counterclockwise. The vortex center will have $|\Gamma_1|$ values >0.9 and =1.0 in the ideal case when the vortex is axisymmetric. In real turbulent flows, the vortex's appearance contains a broad range of irregular shapes. Thereby, we set a threshold for a vortex center $|\Gamma_1| \geqslant 0.75$. More precisely, a point P will be considered as a vortex center if the $|\Gamma_1|$ value is above 0.75 and if it is a local maximum within the region S.

The function Γ_2 considers the contribution of the average local velocity field around the vortex center. The definition of the discrete version of Γ_2 is

$$\Gamma_2(P) = \frac{1}{N}\sum_S \frac{[\boldsymbol{PM} \times (\boldsymbol{U}_M - \overline{\boldsymbol{U}}_P)] \cdot \boldsymbol{z}}{\|\boldsymbol{PM}\| \cdot \|\boldsymbol{U}_M - \overline{\boldsymbol{U}}_P\|}. \quad (2)$$

Here, $\overline{\boldsymbol{U}}_P$ is the local average velocity around the point P, that is,

$$\overline{\boldsymbol{U}}_P = \frac{1}{N}\sum_S \boldsymbol{U}. \quad (3)$$

It can be shown that in the case of incompressible flow, for a very small 2D vortex area ($S \to 0$), function Γ_2 depends on the antisymmetrical and symmetrical parts of the velocity gradient $\nabla\boldsymbol{U}$ tensor at point P. Locally, the flow is dominated by rotation if $|\Omega/\mu| > 1$, which implies $|\Gamma_2| > 2/\pi$. Here, Ω (the rotation rate) and μ (the eigenvalue) correspond to the antisymmetrical part and symmetrical part of the $\nabla\boldsymbol{U}$, respectively. It is important to note that such classification has not yet been defined in the case of a finite region S (Graftieaux et al. 2001).

2.3. Vortex Identification with the Convolution Γ Method

The discrete Γ_1 function for the 2D convolution version of the Γ method (hereafter CGM) was proposed by Zigunov et al. (2020):

$$\Gamma_1(P) = \frac{1}{N}\left[\sum_S \frac{PM_x}{\|\boldsymbol{PM}\|}\frac{U_{My}}{\|\boldsymbol{U}_M\|} - \sum_S \frac{PM_y}{\|\boldsymbol{PM}\|}\frac{U_{Mx}}{\|\boldsymbol{U}_M\|}\right]$$
$$= \frac{1}{N}\left[\frac{PM_x}{\|\boldsymbol{PM}\|} \circledast \frac{U_{My}}{\|\boldsymbol{U}_M\|} - \frac{PM_y}{\|\boldsymbol{PM}\|} \circledast \frac{U_{Mx}}{\|\boldsymbol{U}_M\|}\right], \quad (4)$$

where U_{Mx} and U_{My} correspond to the x- and y-components of the velocity vector starting from the point M within the rectangular region S. Analogously, PM_x and PM_y are the corresponding components of displacement vectors from the point P to a point M. The potential vortex center P is regarded as the origin of this coordinate system defined inside S. The variable N is the number of discrete grid points around the point P within the S region. The "$\circledast$" is the convolution operator. We can write the first terms in the convolutions in a trigonometric representation:

$$\frac{PM_x}{\|\boldsymbol{PM}\|} = \cos(\theta_{PM}), \quad \frac{PM_y}{\|\boldsymbol{PM}\|} = \sin(\theta_{PM}). \quad (5)$$

Thus, the two convolutions in Equation (4) can be represented as multiplications of convolution kernels by the sines and cosines of the angles between the vectors $\boldsymbol{U}_M$ and the x-axis, i.e., $\sin(\theta_{U_M})$ and $\cos(\theta_{U_M})$, respectively (see Zigunov et al. 2020, for more details). Therefore, this equation can be

rewritten as

$$\Gamma_1(P) = \frac{1}{N}\left[\sum_S \cos(\theta_{PM})\sin(\theta_{U_M}) - \sum_S \sin(\theta_{PM})\cos(\theta_{U_M})\right]. \quad (6)$$

In other words, the form presented in Equation (4) is still an analysis of the geometry of the velocity field in the region S. In fact, Equation (6) can be directly recovered from Equation (1) by substituting $\theta_M = \pi - \theta_{U_M} + \theta_{PM}$. The practical advantage of Equation (4) is the use of convolution operations, which enable the use of small convolution kernels within the region S. It is also important to mention that a small convolution kernel helps to identify the vortices that are close to each other, which is difficult to do in the case of the direct use of the Γ_1 function (see Equation (1)).

The full displacement matrix for the x-components of the displacement vectors $\boldsymbol{PM}$ for a small area—for example, 7×7 points M—within the region S can be represented as

$$PM_x = \begin{bmatrix} -3 & -2 & -1 & 0 & 1 & 2 & 3 \\ -3 & -2 & -1 & 0 & 1 & 2 & 3 \\ -3 & -2 & -1 & 0 & 1 & 2 & 3 \\ -3 & -2 & -1 & 0 & 1 & 2 & 3 \\ -3 & -2 & -1 & 0 & 1 & 2 & 3 \\ -3 & -2 & -1 & 0 & 1 & 2 & 3 \\ -3 & -2 & -1 & 0 & 1 & 2 & 3 \end{bmatrix}. \quad (7)$$

Each element of this matrix corresponds to the normalized distance between two discrete points P and each M inside the convolution kernel. The displacement matrix PM_y can be represented as $PM_x^\top$. The general format of PM_x, PM_y, and $\|\boldsymbol{PM}\|$ is shown in Appendix A. The size of these matrices is $(2n + 1) \times (2n + 1)$, where $n \in \mathbb{Z}^+$.

Based on Equation (2), and similar to Equation (4), the convolution version of the Γ_2 function can be introduced as the following:

$$\Gamma_2(P) = \frac{1}{N}\left[\frac{PM_x}{\|\boldsymbol{PM}\|} \circledast \frac{U_{My} - \bar{U}_{py}}{\|\boldsymbol{U}_M - \overline{\boldsymbol{U}}_p\|} - \frac{PM_y}{\|\boldsymbol{PM}\|} \circledast \frac{U_{Mx} - \bar{U}_{px}}{\|\boldsymbol{U}_M - \overline{\boldsymbol{U}}_p\|}\right]. \quad (8)$$

Here, $\overline{U}_{px}$ and $\overline{U}_{py}$ are the x- and y-components of the local average velocity ($\overline{\boldsymbol{U}}_P$) around point P, respectively.

2.4. Advanced Γ Method

Based on the convolution Γ method, we derive the AGM in this section. In Appendix A, we present the general format of the full displacement matrices for the x- and y-components of the displacement vectors $\boldsymbol{PM}$ (PM_x and PM_y). From their structure, we notice that they are rank 1 matrices. This implies that these matrices, for example, PM_x and PM_y, are separable. Therefore, they can be represented as

$$PM_x = \boldsymbol{w}_1 \otimes \boldsymbol{w}_2 \quad (9)$$

and

$$PM_y = (\boldsymbol{w}_1 \otimes \boldsymbol{w}_2)^\top = \boldsymbol{w}_2^\top \otimes \boldsymbol{w}_1^\top, \quad (10)$$

where $\boldsymbol{w}_1$ is a column unit vector and $\boldsymbol{w}_2$ is a row vector. The general format of $\boldsymbol{w}_1$ and $\boldsymbol{w}_2$ of size $2n + 1$ can be represented

as

$$w_1 = [1 \quad \cdots \quad 1 \; 1 \; 1 \; 1 \; 1 \quad \cdots \quad 1]^\top,$$
$$w_2 = [-n \quad \cdots \quad -2 \; -1 \; 0 \; 1 \; 2 \quad \cdots \quad n]. \quad (11)$$

By substituting Equations (9) and (10) into Equation (4), $\Gamma_1(P)$ can be presented as

$$\Gamma_1(P) = \frac{1}{N}\left[\frac{w_1 \otimes w_2}{\|PM\|} \circledast \frac{U_{My}}{\|U_M\|} - \frac{w_2^\top \otimes w_1^\top}{\|PM\|} \circledast \frac{U_{Mx}}{\|U_M\|} \right]. \quad (12)$$

Then, by taking into account that the outer product $w_1 \otimes w_2$ (for the 2D case) can be replaced by the convolution of these two vectors (see Appendix B), we arrive at

$$\Gamma_1(P) = \frac{1}{N}\left[\frac{w_1 \circledast w_2}{\|PM\|} \circledast \frac{U_{My}}{\|U_M\|} - \frac{w_2^\top \circledast w_1^\top}{\|PM\|} \circledast \frac{U_{Mx}}{\|U_M\|} \right]. \quad (13)$$

Similar to the original Γ method, here we consider a small region S, such that the values of $\|PM\|$ (at all the points in S) present only minor variations compared with its mean value. Therefore, $\|PM\|$ at every point can be approximated by a given constant value Z_1; that is, Z_1 replaces the components of the matrix $\|PM\|$ in the region S. This approximation simplifies the calculations, which is needed for the better performance of computation on larger data sets. According to Equation (A2), one may consider that there are some difficulties with satisfying this condition, but later on, in Section 2.5, it is shown that this approximation provides both valid and accurate results.

By applying the commutative and associative properties of the convolution operation, Equation (13) can be represented as

$$\Gamma_1(P, S_1) = \frac{1}{Z_1 N_1}\left[\left(w_1 \circledast \frac{U_{My}}{\|U_M\|} \right) \circledast \right.$$
$$\left. w_2 - \left(w_2^\top \circledast \frac{U_{Mx}}{\|U_M\|} \right) \circledast w_1^\top \right]. \quad (14)$$

Here, we define S_1 as a subset of S (e.g., $S_1 \subset S$) and S_1 is a small enough region to satisfy $\|PM\| \approx Z_1$; N_1 is the number of grid points within the region S_1. The use of Equation (14) has a number of advantages. First, as demonstrated in Section 2.5, there is no need to compute $\|PM\|$. Second, due to the separation of the convolution kernel, the AGM for the calculation of Γ_1 is computationally faster than the CGM (see Equation (4)) by $ks/2$ times, where ks is the kernel size (see Appendix C for more details). The ks represents the dimension of the displacement matrix, for example, PM_x, PM_y. Analogously, Γ_2 can be represented in the following form:

$$\Gamma_2(P, S_2) = \frac{1}{Z_2 N_2}\left[\left(w_1 \circledast \frac{U_{My} - \overline{U}_{py}}{\|U_M - \overline{U}_p\|} \right) \circledast \right.$$
$$\left. w_2 - \left(w_2^\top \circledast \frac{U_{Mx} - \overline{U}_{px}}{\|U_M - \overline{U}_p\|} \right) \circledast w_1^\top \right], \quad (15)$$

where

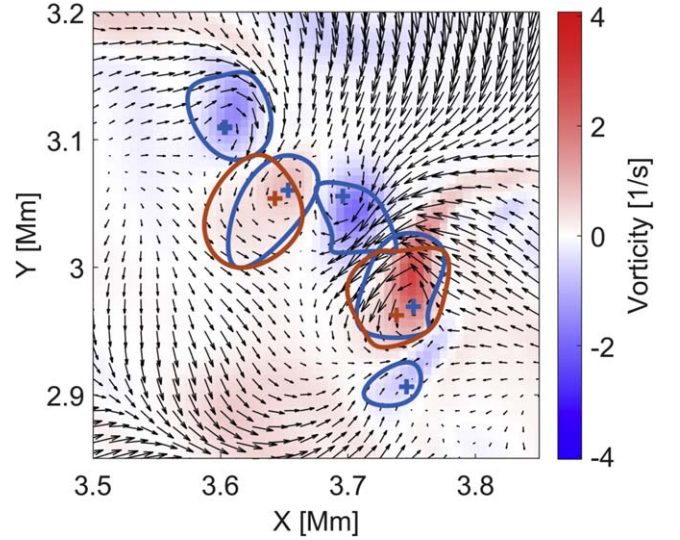$$\overline{U}_P = \frac{1}{N_2}\sum_{S_2} U \quad (16)$$

Figure 2. Vortex detection by the AGM using different kernel sizes (ks). The blue contours (crosses) indicate the vortex boundaries (centers) obtained by applying the AGM with $ks = 3$. The orange contours (crosses) indicate the vortex boundaries (centers) obtained by applying the AGM with $ks = 7$.

is the local average velocity within region S_2 surrounding a point P, N_2 is the number of grid points in the region S_2, Z_2 is the average of $\|PM\|$ inside the region S_P, and $\overline{U}_{px}$ and $\overline{U}_{py}$ are the x- and y-components of the $\overline{U}_p$ defined within region S_2, respectively. The Γ method and the CGM use the same region S for calculating Γ_1 and Γ_2. However, the velocity values at the grid points that are close to the corners of the region S do not significantly influence the true vortex boundary, and, therefore, the use of those points in the average calculation of $\overline{U}_p$ may lead to an unwanted contribution to the Γ_2 calculation. As a result, we apply a different geometry to the subset of the region S— that is, S_2—when calculating Γ_2 in the AGM. For a point P in the domain, the region S_2 includes the vortex center, its boundary, and neighboring regions that truly contribute to the actual value of the local average velocity.

The size of region S_1 is defined in such way that it encompasses only one vortex at each time. In other words, a set of vortices originally found in region S will be separated into individual vortices where each vortical structure is within a region S_1. In order to achieve this, S_1 is set to have the same size as its convolution kernel. Figure 2 presents the detection results obtained by the AGM, using two different single kernel sizes—that is, $ks = 3$ (blue contours) and $ks = 7$ (orange contours)—in a region where multivortices are close to each other. The AGM with $ks = 3$ detected five vortex structures, and the AGM with $ks = 7$ (orange) only detected two of them. It is also clear that the center's locations (indicated by the cross signs) change slightly depending on the kernel size. This is due to the fact that a larger S_1 area, such as the one for $ks = 7$, leads to the contribution of irrelevant flow areas when computing Γ functions, thereby introducing errors.

The boundaries shown in Figure 2 are obtained by applying the advanced Γ_2 method to a different region S_2. The first step in defining S_2 is to consider $S_2 = S_1$; that is, S_2 is rectangular and has the same size as the kernel used for the calculation of Γ_2. In this way, we obtain an initial vortex boundary, which is defined by Γ_2. Then we analyzed the velocity points surrounding point P
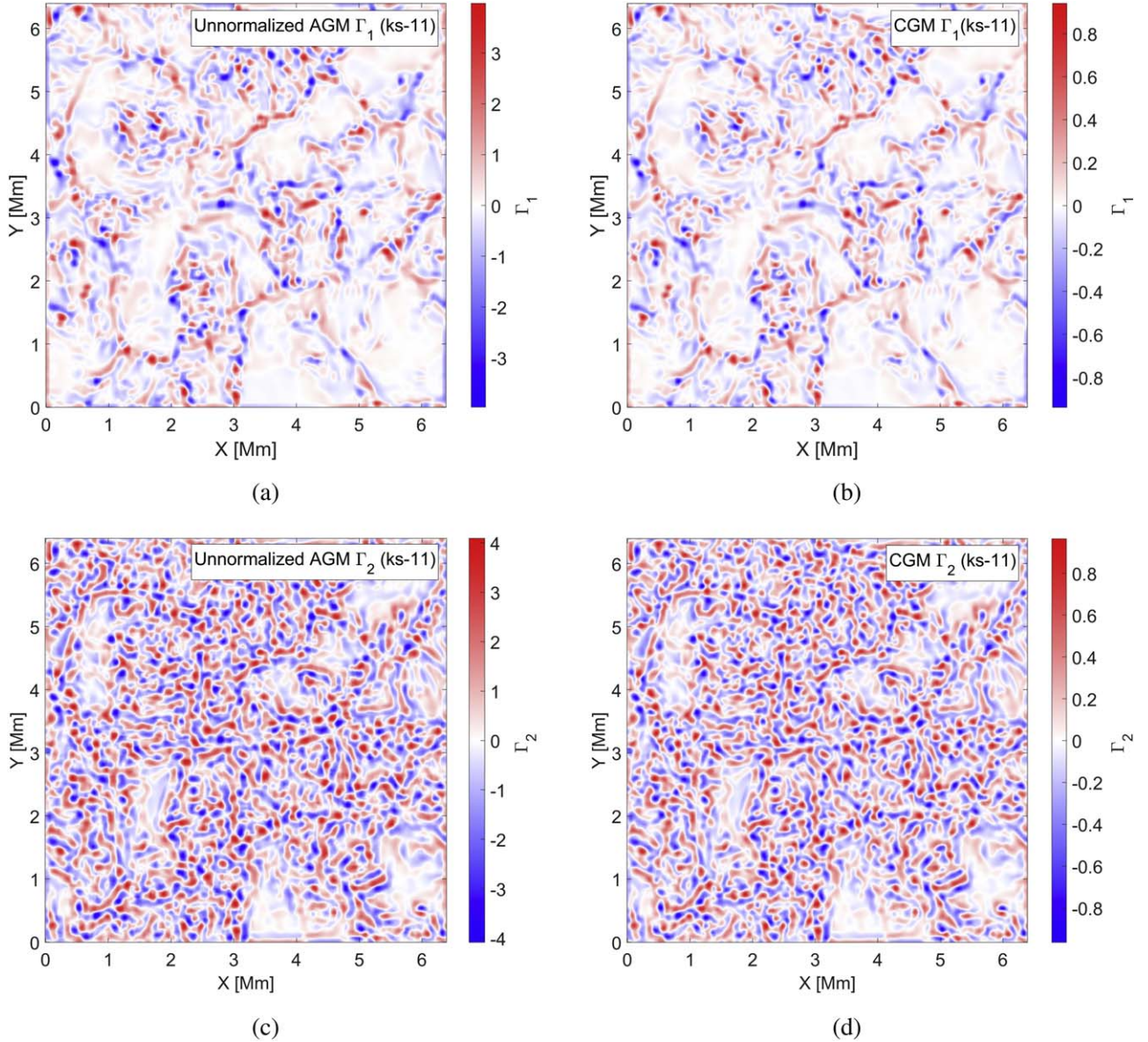
Figure 3. The distributions of the Γ function values obtained by the AGM ((a) and (c)) and CGM ((b) and (d)), which were applied to the photospheric horizontal velocity field, as shown in Figure 1. For both cases, a convolution kernel size $ks = 11$ was applied. As here, the values of Z_1 and Z_2 for the AGM were equal to 1, and the AGM was unnormalized.

just outside the initial vortex boundary. To check whether a point M outside the initial boundary meets the Γ_2 criteria, we recalculate Γ_2 with the changed S_2 region to encompass the M point. In other words, we take into account the M-point contribution to the local $\overline{U}_P$. This procedure is repeated until the points outside the new boundary do not obey the original Γ_2 criteria. The slightly different shapes for the two vortices identified by the use of $ks = 3$ and $ks = 7$ are related to their identified center's location and corresponding customized S_2.

2.5. The Estimation of the Z Value

In order to compare the detection performance between the AGM and the CGM, both were applied to the same magnetoconvection simulation data set (Figure 1). The corresponding values of the Γ_1 and Γ_2 fields calculated for the horizontal velocity field are shown in Figure 3. To analyze the influence of Z_1 and Z_2, first we calculate the AGM using

$Z_1 = Z_2 = 1$, and we call the map of those Γ values the "'unnormalized" AGM (see Figures 3(a) and (c), respectively). For comparison, panels (b) and (d) of the same figure display the results obtained by the CGM. Both the AGM and CGM were applied using the same kernel size $ks = 11$; that is, each separable convolution kernel has the same size of 11×11. Both the AGM and CGM provide the same spatial distribution of Γ_1 and Γ_2 functions, differing only in the absolute values. The CGM provides the same range as the classical Γ method, which is expected, since one can easily recover the original Γ method from CGM functions. The separation of kernels introduced by the AGM changes the maximum and minimum range of its functions if the correct values of Z_1 and Z_2 are not applied, but it does not change the Γ functions' spatial distribution.

Figure 4 presents distributions of ratios (i.e., C_1 and C_2) between the unnormalized AGM and CGM for Γ_1 and Γ_2. The mean values of the C_1 and C_2 distributions are 4.625 and 4.5,
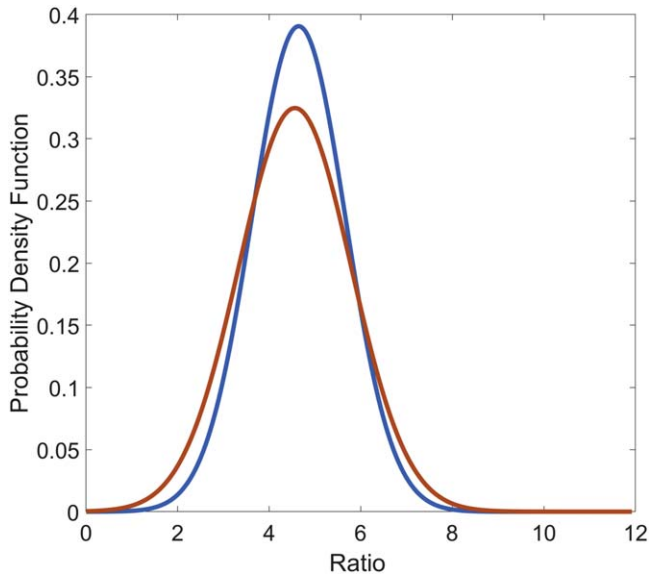
Figure 4. The distributions of the ratios between the unnormalized AGM (Figures 3(a) and (c)) and CGM (Figures 3(b) and (d)) for Γ_1 (C_1 is shown in blue) and Γ_2 (C_2 is shown in red). For both cases, the convolution kernel is equal to 11.
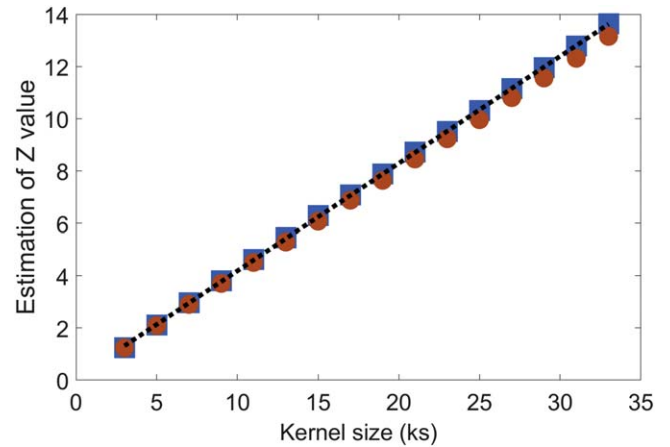

Figure 5. The relationship between the estimated Z values and convolution kernel size (ks). Blue squares indicate the mean ratios of C_1 and orange circles correspond to the mean ratios of C_2. The black dashed line is the linear regression between them.

respectively. In other words, the Γ values detected by the unnormalized AGM are on average $\mu(C_i)$ times larger than the corresponding Γ values detected by the CGM. Therefore, in general, to obtain the AGM within the same range as the CGM for $ks = 11$, one should apply the values obtained for $\mu(C_1)$ and $\mu(C_2)$ to Z_1 and Z_2, respectively. The variance of the $C_{1,2}$ distributions reflects how good the approximation provided by the $Z_{1,2}$ values to the $\|\boldsymbol{PM}\|$ values is; that is, if Var $(C_{1,2}) = 0$, $Z_{1,2}$ is identical to $\|\boldsymbol{PM}\|$. In Appendix D, we present the same analysis for the case $ks = 33$.

Figure 5 presents a series of mean ratios of C_1 (blue squares) and C_2 (orange circles) versus the corresponding size of the convolution kernel (ks). Both dependencies show near-linear behavior, which indicates that the mean ratio increases with ks.

Based on the analysis performed, we can conclude that Z_1 and Z_2 can be chosen to be equal to the mean values of C_1 and C_2. In other words, such assumptions will provide the AGM functions within the expected range of −1, 1. Moreover, in cases where the difference between Z_1 and Z_2 is small enough, one can set $Z_1 = Z_2$, which can simplify the algorithm further. Our results also indicate that the selection of kernel size will influence the detection efficiency (see Equation (C1)) and accuracy. For instance, by comparing Figures 3 and 19, we have found that the small-scale processes are better captured in Figure 3.

The vortex detection by the AGM can be optimized by using an adaptive version of the AGM, which is based on a sequence of different kernel sizes, for example, 3, 5, 7, 9, and 11, and so on. Ideally, the kernel is located at the center of the potential vortical structure. For small odd-size kernels—that is, $ks = 3$—this may lead to nondetection (a failure to detect), and the use of a sequence of growing kernel sizes increases the chance of detection. This is illustrated in Figure 6(a), where the AGM with $ks = 5$ detected the vortex center (blue cross) outside the grid points. The same region would have a Γ_1 value lower than the threshold when applying the AGM with $ks = 3$, as illustrated in Figure 6(b), where the corresponding Γ_1 values of the grid points surrounding the

vortex center are indicated with black dashed arrows. The blue and red dashed squares show two kernel domains that can be applied when calculating the corresponding Γ_1 values. When the kernel size increases to $ks = 5$, which is depicted in Figure 6(c), the Γ_1 value is above the threshold and the vortex center is finally detected.

As discussed above, several kernel sizes may yield values of Γ_1 greater than the threshold; therefore, the result with the maximum value of Γ_1 will be selected to be the detection result. The maximum of the Γ_1 value indicates the most accurate location of the vortex center, as illustrated by Figures 2 and 6. As the vortex boundary is influenced by the kernel size (see Figure 2), the final area of the vortex is affected by the choice of the kernel. Therefore, some statistical features of the vortex, like the size and center properties, are affected as one applies the most appropriate kernel size to describe a given vortex. For example, larger kernel sizes are better suited to describe vortices presenting greater areas and the opposite is found for small kernels. Therefore, varying the kernel size for each vortex, as done by the adaptive AGM, provides us with better identification and leads to the more accurate statistical results of the vortex parameters.

3. Vortex Detection Results and Statistical Analysis

In this section, the vortex detection was performed with the use of the AGM method with a maximum of five different convolution kernel sizes. The candidate for a vortex center is located at the center of the kernel, and, therefore, it is surrounded by an even number of grid points in the x- and y-directions, which correspond to $ks = 3$, 5, 7, 9, and 11. For convenience, we set $Z_1 = Z_2$ (see Section 2.5). For different kernel sizes, the values of Z_1 and Z_2 were set equal to the values of the linear regression function (see Figure 5). For example, for $ks = 11$, these values correspond to $Z_1 = Z_2 = 4.597$. The threshold of $|\Gamma_1|$ is set equal to 0.75. As in the classical Γ method, a candidate for a vortex center will be considered a true center if $|\Gamma_1| > 0.75$ and if the $|\Gamma_1|$ value at that point is larger than in the other surrounding grid points. Similarly, for Γ_2, we apply the threshold of $2/\pi$.
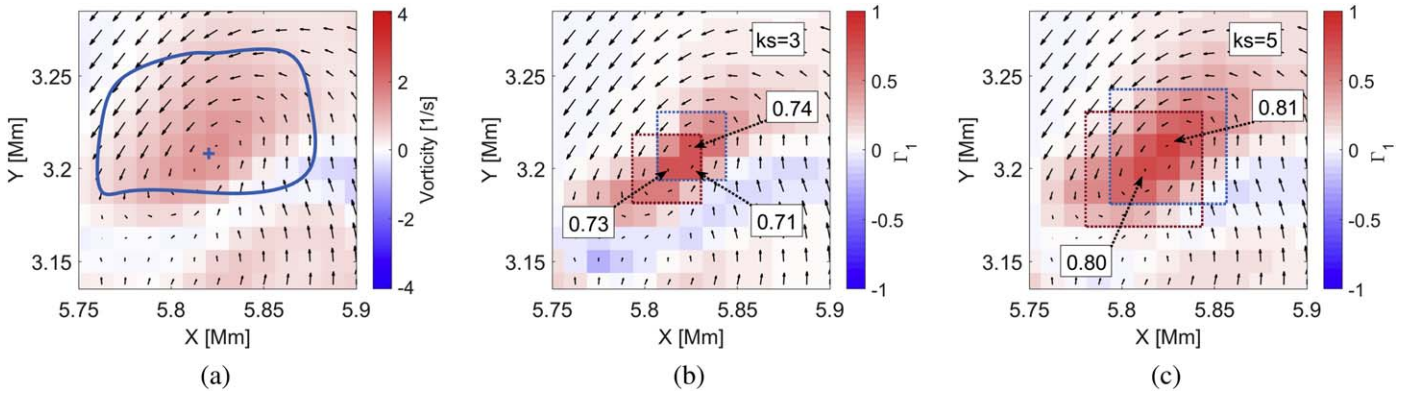
Figure 6. (a) Vortex detected with the adaptive AGM. The vortex center and boundary are indicated with the blue cross and contour, respectively. (b) The Γ_1 map detected with $ks = 3$ of panel (a). The blue and red squares indicate the two 3×3 kernel domains that were used to calculate Γ_1. (c) The Γ_1 map detected with $ks = 5$ of panel (a). The blue and red squares indicate the two 5×5 kernel domains that were used to calculate Γ_1.

3.1. Detection Results

The AGM algorithm was applied to the whole simulated photospheric velocity field (see Figure 1), but here we will focus on the detection results of a single vortex. Figure 7 shows the identification obtained by applying the AGM with $ks = 7$. In all the panels, the vortex boundary is indicated by a red curve, and we see that the AGM provides a boundary that aligns well with the velocity streamlines (shown in blue). Based on the velocity field arrows (shown in black), it is clear that the vortex center, represented by a red cross, is also well detected by the AGM. The radial velocity component changes sign with the flow, as displayed in panel (a), and the tangential velocity component decreases from the boundary toward the center (see panel (b)). As expected, the vortex covers the area with the maximum vorticity, panel (c), and the high value of the angular velocity component, panel (d). In particular, this vortex is located in a downflow region, panel (e), and in the region of the low compressible plasma, panel (f).

The averaged (over angular directions) radial and tangential velocity profiles as a function of time and radius for the vortex shown in Figure 7 are shown in Figures 8(a) and (b), respectively. The vertical axis represents the distance from the vortex center to the mean maximum vortex radius (green dashed line), and the horizontal axis indicates the lifetime scale of the vortex. The radial and tangential velocity components show a maximum value just after the vortex appearance, and then they tend to decrease as the vortical structure disappears. The value of the tangential velocity component is approximately five times larger than the corresponding radial velocity component. Furthermore, the tangential component has larger values closer to the boundary; that is, plasma decelerates as it approaches the center. This result is in good agreement with previous results (Silva et al. 2020). The change in sign of the radial velocity component close to the average boundary (see Figure 8(a)) indicates that the AGM detection might have slightly overestimated the vortex boundary.

The AGM identifies vortices at each time frame, but it does not automatically provide the time evolution of a detected vortical structure. To analyze the vortex behavior during its lifetime, it is necessary to make sure that tracking of the vortex center and boundary is applied to the same vortex over a period of time. To satisfy this, it was assumed that the maximum displacement distance of the vortex center between two

successive frames of this numerical simulation would be 50 km (equivalent to four pixels of the simulation grid). This strategy is based on Giagkiozis et al. (2018), where the speed of the vortex center was assumed to be near the speed of sound in the photosphere (i.e., 10 km s^{-1}, given by Nordlund et al. 2009). Therefore, if in two consecutive frames a vortex center is detected within 50 km from another vortex center in the previous frame, they are the same vortical structure.

The temporal evolution of the boundary and center of vortex number 1 is presented in Figure 9. The position of the vortex center is mostly oscillating during its lifetime (i.e., between t_0 and t_7) around the initial position. This means that the vortex does not show significant displacement in space. The boundary tends to shrink close to the end of the vortex lifetime (t_7). The decrease in the vortex area is shown in Figure 9(b). The blue and orange curves depict the area and average radius of the vortex as functions of time, respectively. An identified average radius around 35–45 km is in accordance with previous findings for lower photospheric vortices in MURaM magnetoconvection simulations (Silva et al. 2020; Aljohani et al. 2022). The vorticity and Γ_1 as functions of time are shown in Figure 9(c). This result can be explained in the following way. The vorticity does not start at zero, due to the fact that the velocity field lines start to curl even before the detection by Γ_1. Due to the threshold, the vortex is only considered to start to exist when its Γ_1 is greater than the threshold. Close to the end of its lifetime, there is a steep decrease in the vorticity magnitude, which starts at $t_5 = 30$ s, close to the vortex decay at $t_7 = 40$ s. As expected, the Γ_1 value (orange curve) shows a similar behavior.

3.2. Statistical Results

First, to evaluate how different kernel sizes affect the statistics of the identified vortices, the AGM with $ks = 3$, 7, and 11 and the Γ method were applied to the same simulation data. Figure 10 summarizes the obtained results. The green, yellow, and purple curves correspond to the results of AGM $ks = 3$, 7, and 11, respectively. The blue curve indicates the instantaneous detection result by the adaptive AGM. The Γ method identification results are shown in red. All results show a similar curve trend as a function of time, but they provide a different number of detections. Among the different ks applied for the AGM, the lowest average number of vortex detections
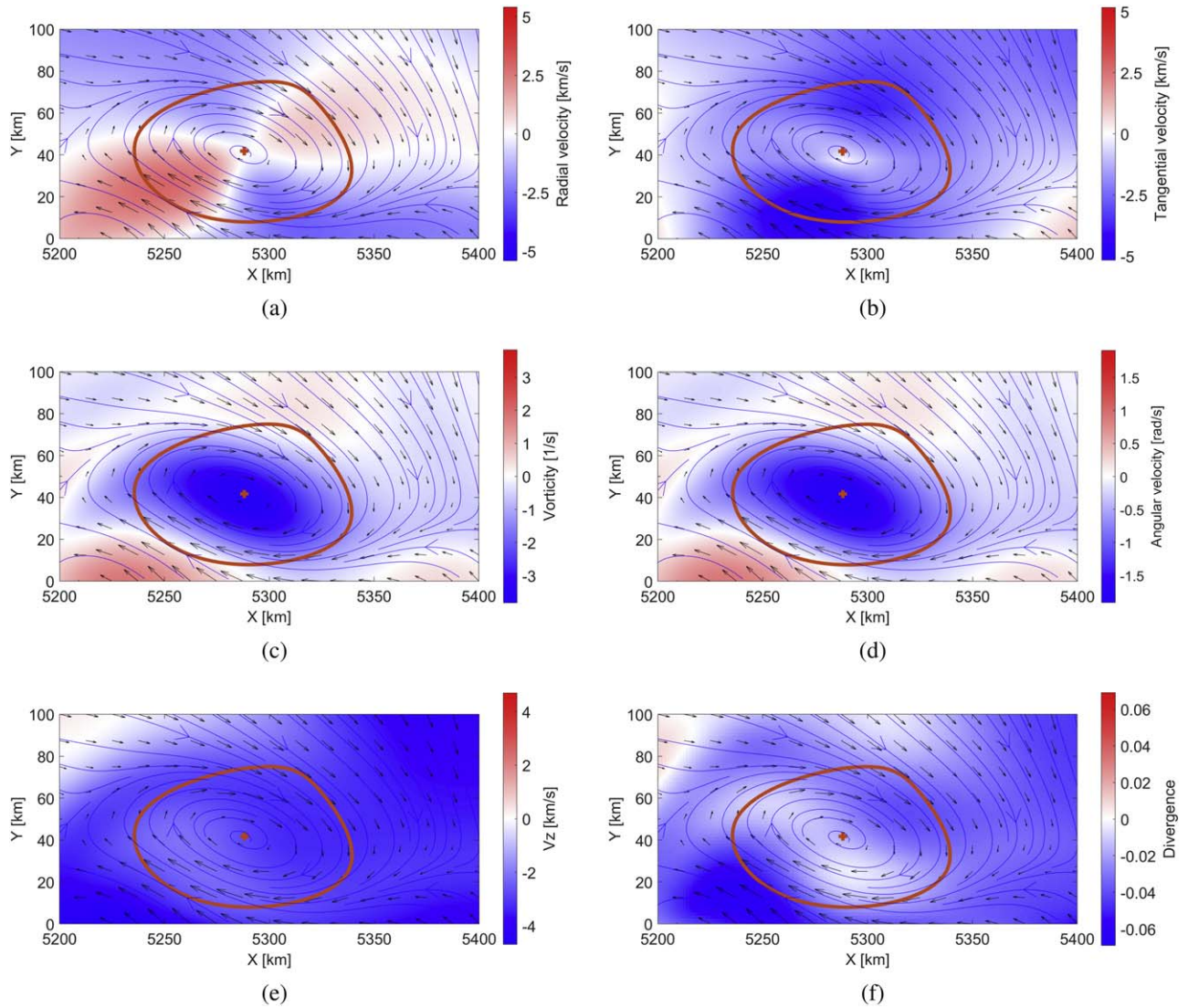
Figure 7. The vortex number 1 as it was detected by the AGM using $ks = 7$ at the moment $t = t_0$. The orange plus sign indicates the vortex center, and the orange contour depicts the corresponding boundary. The direction of the horizontal velocity field is indicated by the streamlines and the arrows in blue. The background is colored by (a) the radial velocity component, (b) the tangential velocity component, (c) the vorticity, (d) the angular velocity component, (e) the vertical component of the velocity field, and (f) the divergence of the velocity.

—that is, on average, 51.1 at each time frame—is obtained when using $ks = 11$, followed by $ks = 7$, with 95.1 detections, and $ks = 3$, with 124.6 detections. The Γ method presents results similar to the AGM with $ks = 3$, with an average detection number of 112.4. The higher number of detected vortices by the adaptive AGM appears to be due to the use of different kernel sizes in the same region of interest (ROI). This makes it possible to detect vortices even if they are very close to each other. By comparing the total number of detected vortices, it was found that the Γ method detects only 69.7% of the actual vortical structures in the ROI compared with the AGM. The AGM $ks = 3$ identifies 77.3%, while AGM $ks = 7$ and AGM $ks = 11$ identify 59% and 31.6%, respectively. These percentage values can be used to provide an estimate of the actual number of vortical structures present in the photospheric flow and also the number of nondetections of each method applied.

In total, 3390 vortices were identified for a time interval of 625 s by the adaptive AGM. Most of the detected vortices tend to anchor around a local region with slight spatial displacement during their lifetime. Figure 11(a) shows the spatial and temporal behavior of a number of identified vortices in the ROI. The evolutions of their boundaries and centers are plotted as a function of time (vertical axis). A zoom-in of the selected area (3×3 Mm) is shown in Figure 11(b). Identified vortical motions have similar behaviors to vortex number 1 shown in Figure 9; that is, little spatial displacement in time and a tendency toward boundary shrinking. The majority of the detected vortices have a lifetime below 50 s, which justifies why it is hard to see 150 vortices in Figure 11. We have only two vortices presenting lifetimes larger than 200 s, which is in accordance with previous studies, for example, Giagkiozis et al. (2018) and Silva et al. (2021). From Figure 10, it is clear that the number of instantaneous detections of vortices by the AGM is larger than the detections by the Γ method, but, at the same time, the lifetimes of the vortices detected by the AGM are also larger. Therefore, the total number of vortices detected by the AGM (3390) is not considerably larger than the number detected by the Γ method (3211).
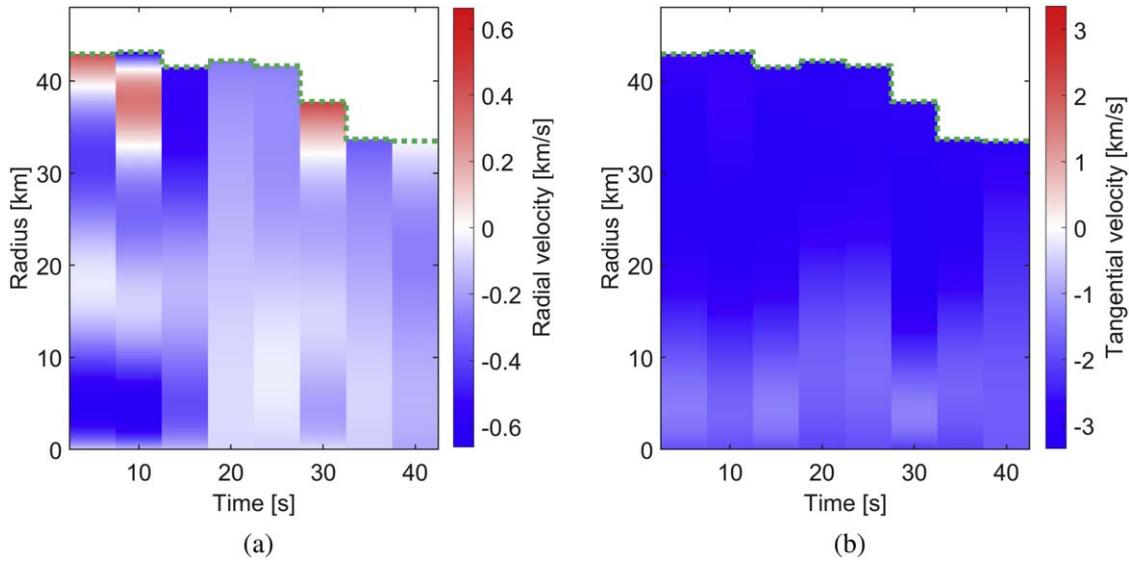
Figure 8. The radial and tangential velocity components (averaged over angular directions) as a function of time and radius are shown in panels (a) and (b), correspondingly. The vertical axis indicates the distance from the vortex center to the mean vortex radius calculated at the corresponding time (green dashed line). The horizontal axis indicates the lifetime scale of the vortex shown in Figure 9.
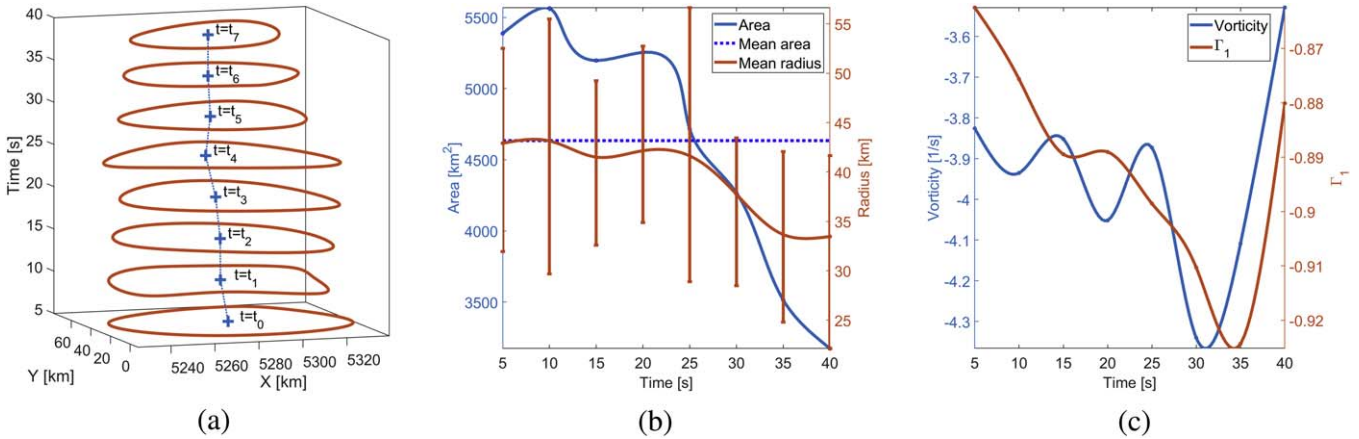

Figure 9. The time-dependent behavior of vortex number 1, which is shown in Figure 7. (a) A series of detected centers of the vortex (blue plus signs) and its boundaries (orange contours) are shown for times $t_0 - t_7$, from the bottom to top. (b) The evolution of the vortex area (blue curve) and mean radius (orange curve). The error bars show the maximum and minimum of the radius at the corresponding time. The dark blue dashed line indicates the mean area of the vortex. (c) The evolution of the vorticity at the center of the vortex (blue curve) and the corresponding evolution of the Γ_1 value (orange curve).
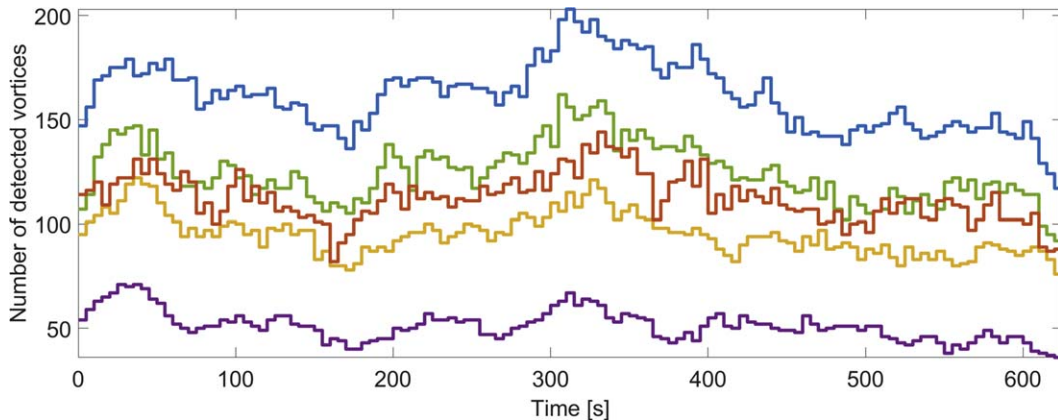
Figure 10. The instantaneous number of vortices detected by the AGM with the use of different kernel sizes: $ks = 3$ (green), $ks = 7$ (yellow), and $ks = 11$ (purple). The results obtained by the adaptive AGM ($ks = 3, 5, 7, 9,$ and 11) are shown in blue, and those by the Γ method are shown in red.
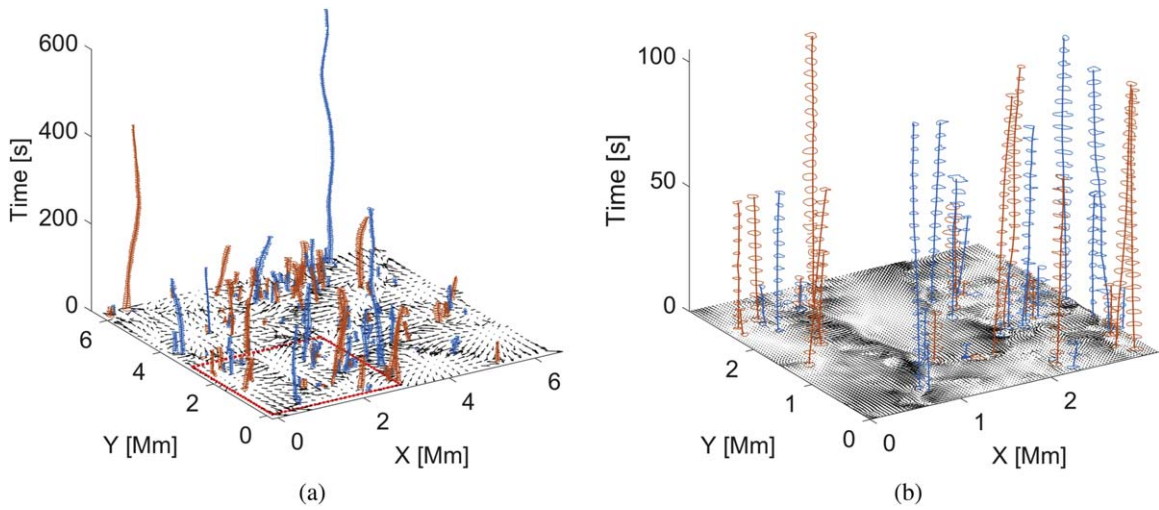
Figure 11. Time evolution of 150 detected vortices (some of them are less visible, due to their short lifetimes; see Figure 12) in simulation data. The size of the analyzed region is 6.4 Mm × 6.4 Mm. The vertical axis indicates the time, and the black arrow indicates the horizontal velocity field at the initial moment of time. The vortices were detected by the AGM using kernel sizes 3, 5, 7, 9, and 11. The orange and blue contours indicate clockwise and counterclockwise rotation vortices, respectively.
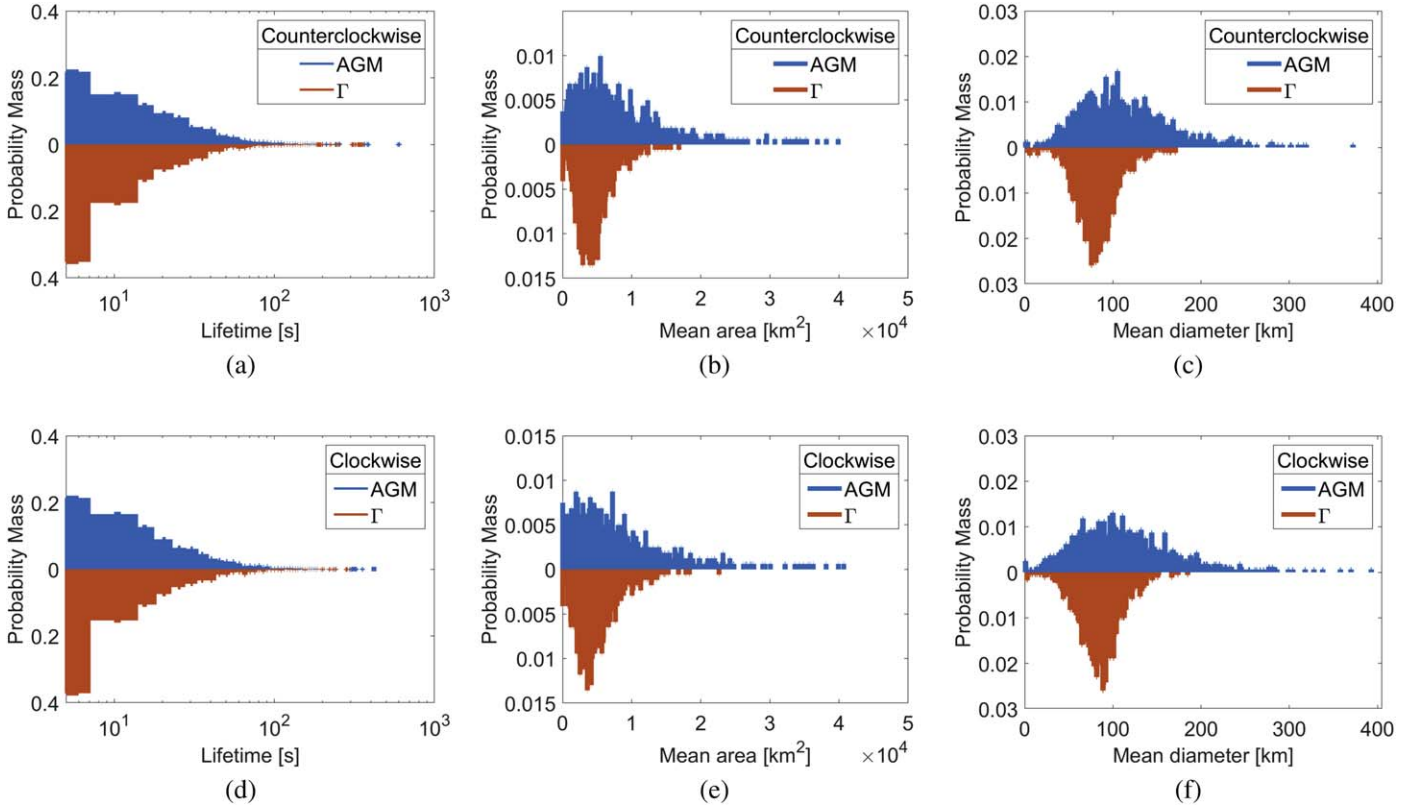
Figure 12. Statistical comparison between vortices detected by the AGM (blue) and the Γ method (red) in numerical data. (a) Probability mass function of the lifetimes of detected counterclockwise vortices. (b) Probability mass function of the mean area of detected counterclockwise vortices. (c) Probability mass function of the mean diameter of detected counterclockwise vortices. (d) Probability mass function of the lifetimes of detected clockwise vortices. (e) Probability mass function of the mean area of detected clockwise vortices. (f) Probability mass function of the mean diameter of detected clockwise vortices.

3.3. Comparison of Identification Results Obtained by the AGM and the Γ Method

In this section, we compare the vortex detection performance between the adaptive AGM and the Γ method. Figure 12 shows the distributions of various vortex parameters—that is, lifetime, mean area, and diameter—detected by the adaptive AGM (shown in blue) and the Γ method (shown in red). These distributions were obtained by analyzing of 625 s of numerical data. The top panels, that is, Figures 12(a)–(c), show the distributions of counterclockwise vortices, and the bottom panels (d)–(e) depict the clockwise-direction vortices. The adaptive AGM detected slightly more vortices than the Γ method; that is, 3390 versus 3211, respectively. The ratio between the counterclockwise and clockwise vortices is nearly 1:1: the AGM identified 1697
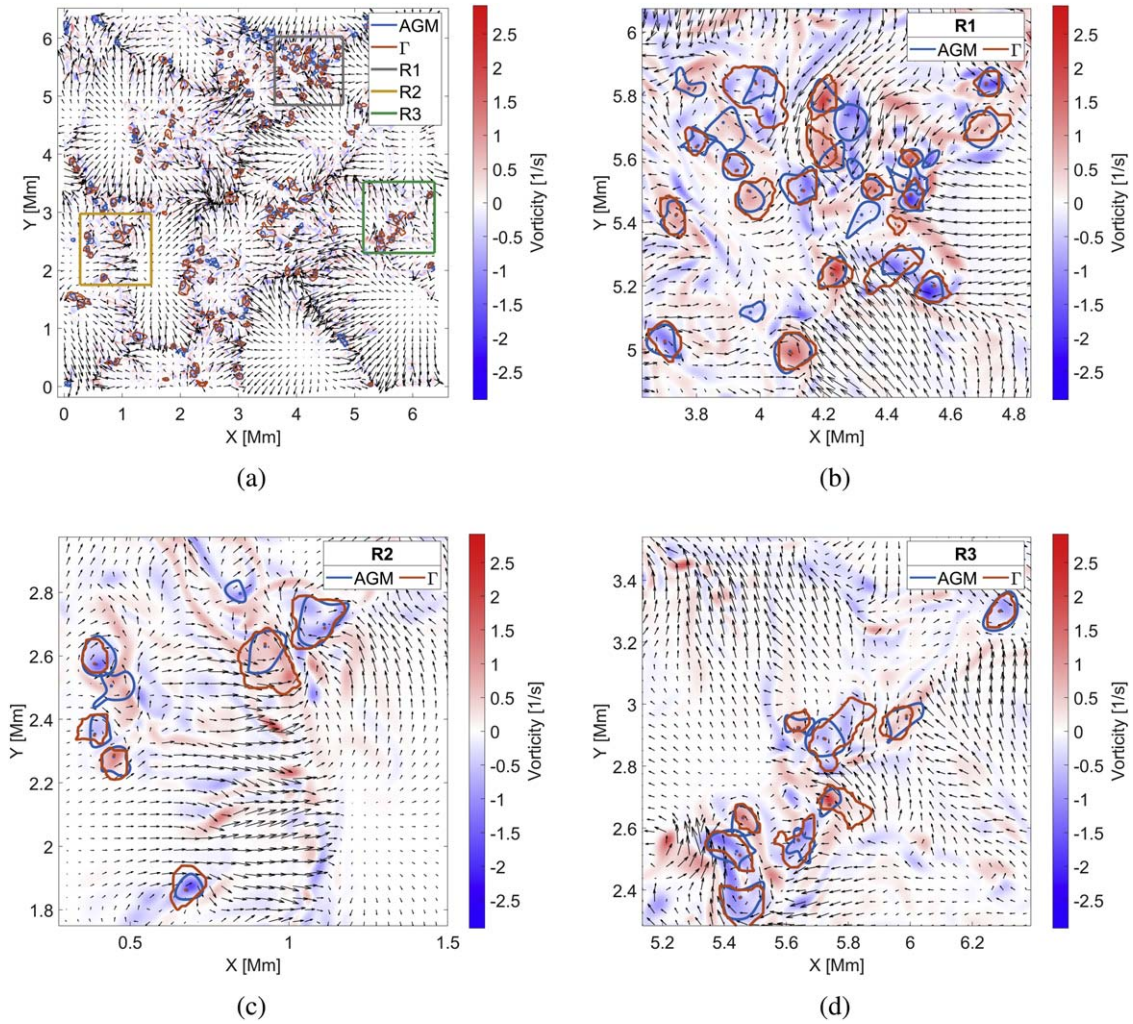
Figure 13. Comparison of detected results between the adaptive AGM method and the Γ method. The blue and orange contours indicate vortices detected by using the adaptive AGM and the Γ method, respectively. Blue dots indicate vortex centers identified by the AGM, while orange dots indicate those identified by the Γ method. The black arrow indicates the horizontal velocity field. Three ROIs (R1, R2, and R3) were selected to zoom in on and are presented with the details in (b), (c), and (d). (a) Spatial domain when time $=35$ s. (b) Zoom-in view of region R1. (c) Zoom-in view of region R2. (d) Zoom-in view of region R3.

counterclockwise and 1693 clockwise vortices; the Γ method detected 1608 counterclockwise and 1603 clockwise vortices. It is clear that the distributions for the detected number, lifetime, mean area, and diameter are independent of the vortex's direction. There are small differences at the tails of the distributions; however, these may appear due to the limitations of the sizes of our time sequences and do not represent the real physical properties of the vortices. The average lifetimes of the detected vortices are 29.72 s for the adaptive AGM and 21.82 s for the vortices detected by the Γ method. This difference relies on the fact that the AGM performs better on the identification of both small- and large-scale vortices when varying kernel size. As it has been shown, close to its lifetime, the vortex tends to shrink and a small convolution kernel enables the AGM to capture this behavior better than the Γ method. Also, the vortex may start at a smaller size that is not easy to capture by the Γ method.

The mean area distributions are shown in Figures 12(b) and (e), and they display nearly Gaussian distribution behavior. The vortex's mean area as detected by the Γ method is 7.28×10^3 km^2 and the corresponding value given by the AGM is 4.67×10^3 km^2. On the other hand, the tail distribution

indicates that the AGM has a higher number of detections presenting larger areas. Another pair of Gaussian-like distributions is obtained for the mean diameter of the detected vortex, as depicted in Figures 12(c) and (f). The AGM gives a smaller value of the detected vortex's mean diameter than the Γ method; that is, AGM, 83.51 km versus Γ, 110.31 km.

The differences in sizes and shapes for vortices detected by the AGM and the Γ method are illustrated in Figure 13, which presents the detections obtained for a selected time frame, $t = 35$ s. The color bar indicates the vorticity scale of the region, and the arrows indicate the direction of the horizontal velocity. The AGM detection is depicted in blue, and the Γ method vortex identification is shown in red. We selected three ROIs, that is, R1, R2, and R3, for comparison. The AGM-detected vortex boundaries were always smoother than those provided by the Γ method, and most of the AGM detections do not overlap, even if vortices are near each other. The Γ method exhibits a sparse detection result within the same region; that is, it has a number of nondetection issues when the vortices are too close to each other. Also, the Γ method tends to overestimate the vortex region compared with the AGM, but it also depends on the chosen threshold value.
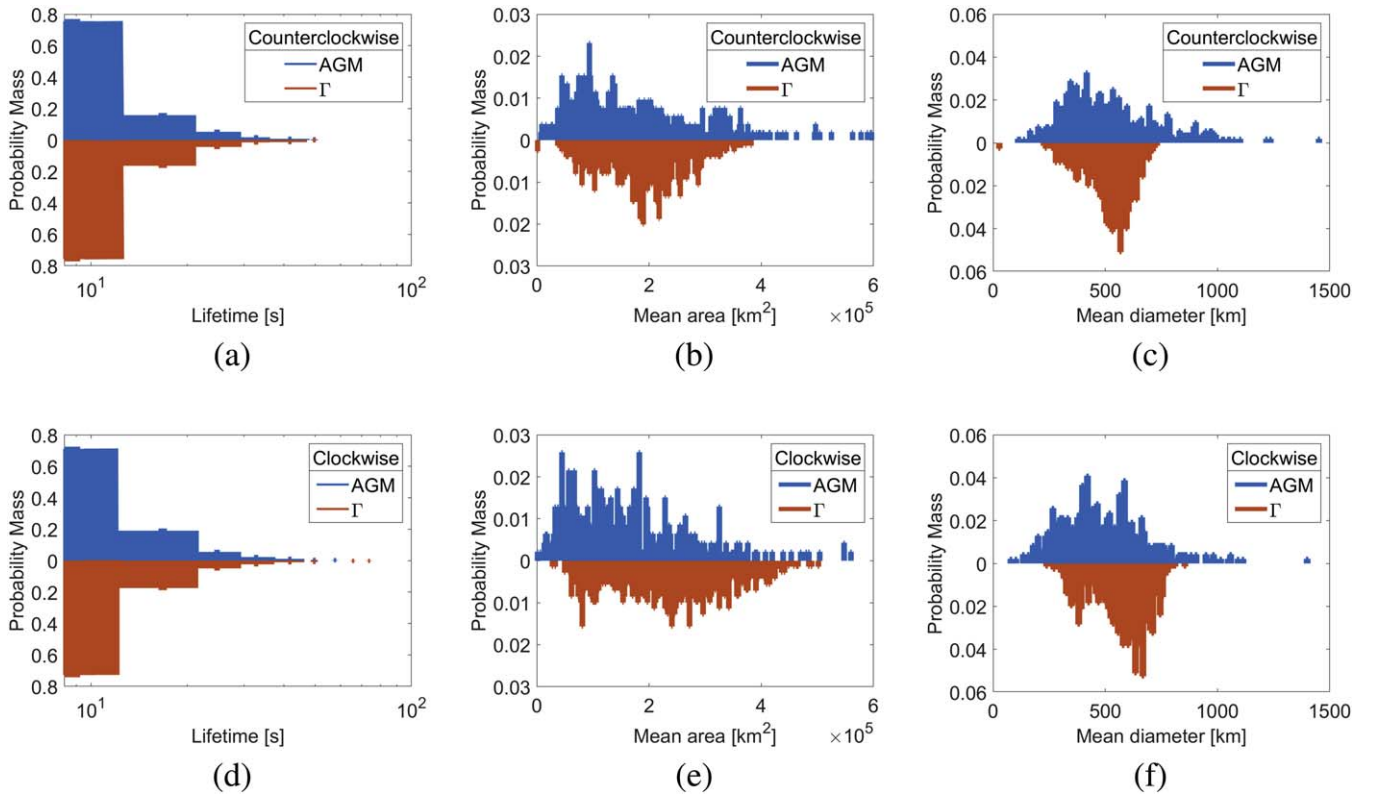
Figure 14. Statistical comparison between vortices detected by the adaptive AGM (blue) and the Γ method (red) in observational data. Three results are shown: lifetime probability mass function of the detected counterclockwise (a) and clockwise (d) vortices; mean area probability mass function of the detected counterclockwise (b) and clockwise (e) vortices; and mean diameter probability mass function of the detected counterclockwise (c) and clockwise (f) vortices.

3.4. Comparison of Observational Data Analysis with Numerical Data Results

In order to test the performance of the adaptive AGM method on high-resolution observational data, we used the data set from the CRISP instrument mounted on the Swedish 1 m Solar Telescope (Scharmer et al. 2003, 2008). The identification results were compared with the results of the Γ method applied to the same observational time sequence. The analyzed data were collected between 08:07:24 and 09:05:46 UT on 2012 June 21, with resolution $0''.059$ per pixel with a mean cadence of 8.25 s. Only part (8.5×8.5 Mm) of the whole domain ($55'' \times 55''$), with a of duration 2425.5 s, was selected for analysis. The adaptive AGM detected 1449 vortices within the ROI, with 709 clockwise and 746 counterclockwise vortices. In contrast, the Γ method detected 982 vortices (464 clockwise and 518 counterclockwise). The ratio between the number of vortices with different directions of rotation (clockwise/counterclockwise) is similar for both methods; that is, 0.95 for the advanced AGM and 0.9 for the Γ method. Therefore, the flexibility of utilizing different kernel sizes in the adaptive AGM when analyzing observational data shows good improvement in the identification of small-scale vortices, especially those with weak vorticity, which may be missed by the Γ method. This is similar to the results obtained from the analysis of numerical magnetoconvection simulations (see Section 3.3).

The mean lifetimes of the vortices detected by both methods are nearly equal, with 11.79 s for the adaptive AGM and 11.68 s for the Γ method. We also found that the mean area of the vortices detected by the adaptive AGM (0.164 Mm²) is comparable to the mean area of the vortices detected by the Γ method (0.2 Mm²). Additionally, the adaptive AGM provided a smaller mean vortex diameter than the Γ method; that is, 504 km and 540.5 km, respectively (see Figure 14).

Comparison of Figures 12 and 14 shows that the ability of the adaptive AGM to detect smaller and larger-scale vortices is preserved even in the case of more irregularly shaped vortices. Although the observation data have a lower resolution (42.75×42.75 km²) compared with the numerical data (12.5×12.5 km²), the mean lifetimes of the vortices found by both methods are rather similar. The observed vortex lifetimes are most likely longer since crucial parts of the vortex lifetimes (the beginning and end) are missed by the lower resolution. A key difference found between the results of the numerical and observational analysis is that the number of detected vortices in the CRISP data is around 12 times smaller than that obtained from the StellarBox simulations (see Figures 10 and 15). This is in accordance with the difference in the spatial resolution, as the resolution of the simulation data is approximately 12 times higher than that of the observational data. Figure 16 shows the identified vortices in the observational data at $t = 231$ s. Zoom-in views of the three selected regions, namely, R1, R2, and R3, are shown in panels (b), (c), and (d). The adaptive AGM provided more precise vortex detection and showed better performance in comparison with the Γ method in regions with a weak vorticity (see Figure 16(d)).

4. Conclusions

In this work, we have presented a new and improved method for vortex identification, based on the previously proposed Γ method (Graftieaux et al. 2001). The CGM (Zigunov et al. 2020)
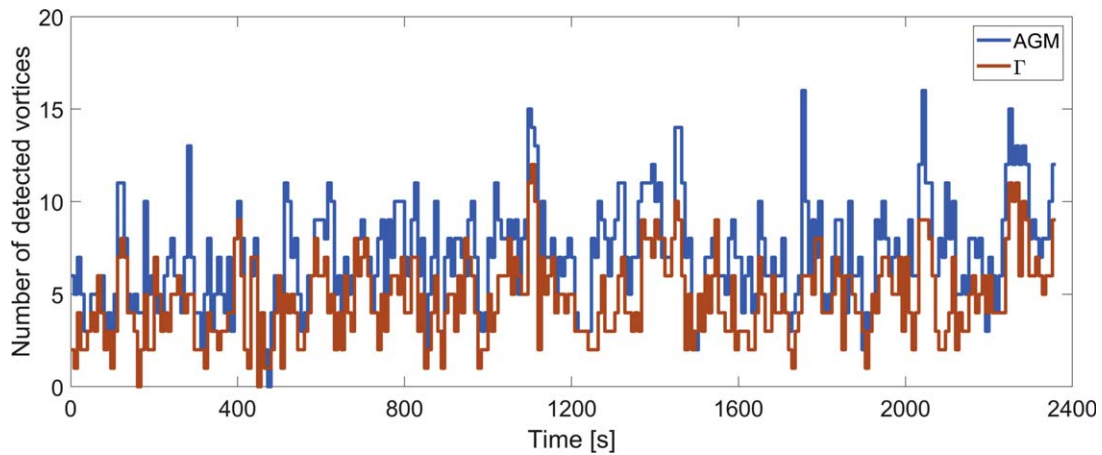
Figure 15. The instantaneous number of vortices detected in the observational data (CRISP) by the adaptive AGM and the Γ method. The results obtained by the adaptive AGM with kernel sizes $ks = 3, 5, 7, 9$, and 11 are shown in blue, and those obtained by the Γ method are shown in red.
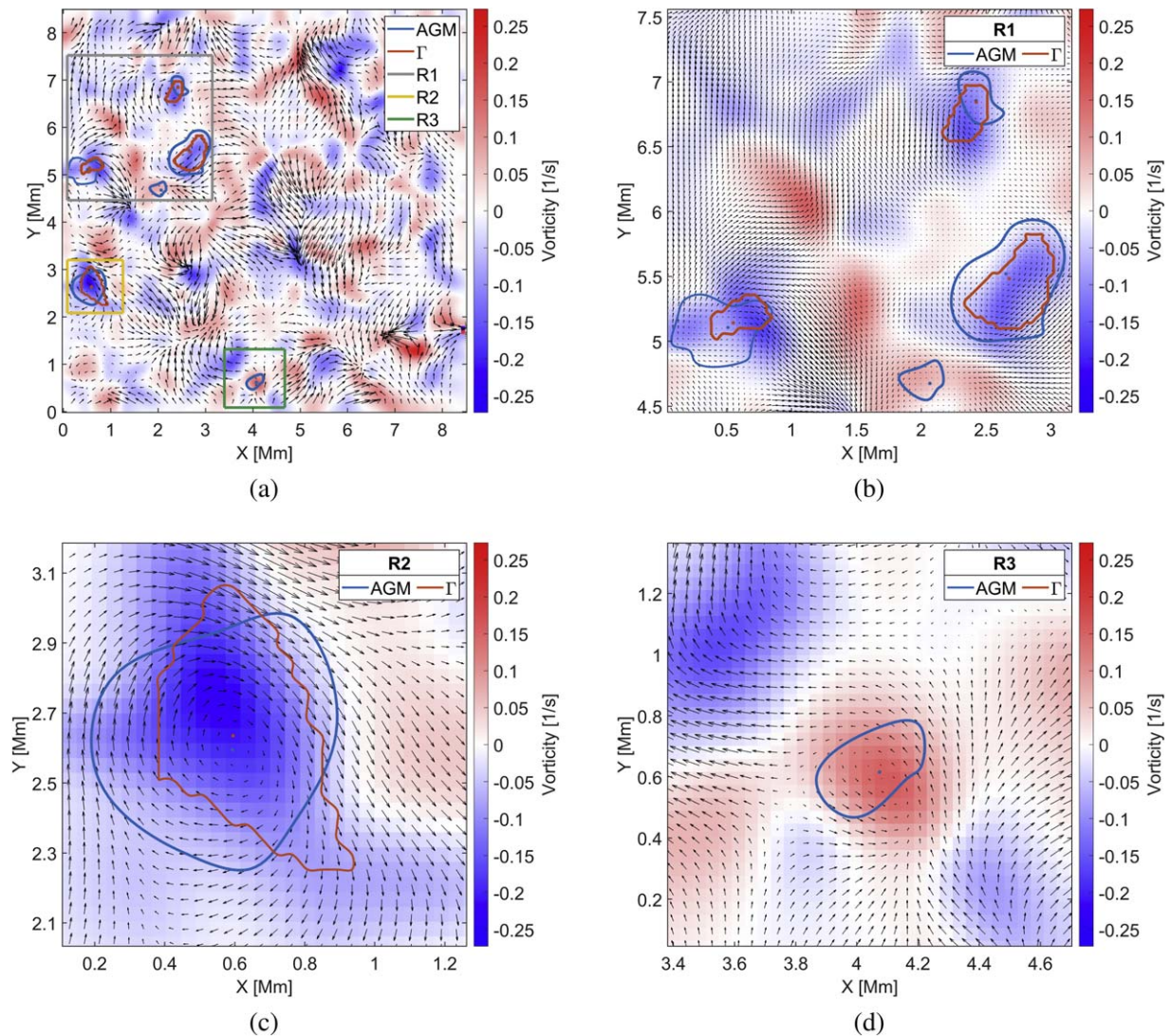

Figure 16. Results of vortex detections by the adaptive AGM and the Γ method. Both methods were applied to observational (CRISP) data at $t = 231$ s (a). The blue and red contours indicate vortices detected by the adaptive AGM and the Γ method, respectively. The detected vortex centers from both methods are shown in blue and red colors as well. The black arrows indicate the horizontal velocity field. Three ROIs (R1, R2, and R3) are selected to zoom in on and are presented in panels (b), (c), and (d).

was extended to provide Γ_2 functions, and the CGM was used to develop the AGM. We have proved that the CGM is mathematically the same as the Γ method and that the AGM provides similar maps to the CGM. The advantage of using the AGM relies on choices of kernel sizes, which allow the detection of vortices at both small and large scales. Moreover, the adaptive AGM, which uses different kernel sizes for identification, provides a smoother and more accurate vortex center and a smoother boundary and is more successful at preventing nondetections. For better identification results, the Γ method requires the customized tuning of parameters separately; that is, for small- and large-scale vortices. Hence, this method is onerous and may lead to overfitting for a specific vortex. Since the AGM is better suited to detecting both small-scale and large-scale vortex behavior, the values of the mean area and diameter given by the AGM are more reliable. Note that the adaptive AGM algorithm selects the optimal vortex profiles and produces the most accurate results, but is more computationally expensive. Although the AGM limits the nondetections caused by threshold choices, there are still limitations on the detections caused by the application of the threshold. More precisely, to be considered as a vortex center, the grid point should present a minimum curl of velocity field lines, and this may lead to the nondetection of weak vortices. Another issue is that it is based on the Γ method, which was developed for divergence-free flows, and therefore the AGM may not work as well in compressible plasma. However, both Giagkiozis et al. (2018) and our results indicate that the Γ method and the AGM perform well in the flow conditions found in the solar atmosphere.

Using the adaptive AGM, we detected and analyzed vortices from a numerically simulated photosphere obtained using the 3D radiative MHD code StellarBox (see, e.g., Kitiashvili et al. 2012; Wray et al. 2015). We found that the vortical structures had a size, a mean radius of about 41.75 km, which was similar to previous vortex studies based on MURaM simulation (Silva et al. 2020; Aljohani et al. 2022). Therefore, our results suggest that the different vortex detection methods were comparable in calculating the average vortex size. However, the tail distributions of the mean radius indicate that the Γ method and the AGM lead to considerable differences in the maximum sizes of the vortices detected in the photosphere. Another discrepancy was found for the average lifetimes, as the adaptive AGM indicated an average lifetime that was much shorter than the one found using IVD in MURaM data (Silva et al. 2021). Those differences may be due to distinct definitions proposed for vortices by different methods, as well as the particularities of the simulation configurations. For instance, Giagkiozis et al. (2018) applied the Γ method to an observational data set and found the average lifetime of the detected vortices to be around 17 s, whereas applying the same methodology to StellarBox data, we found 21 s. However, in all the studies there is a general tendency toward most of the vortices being short-lived, regardless of the type of data set or identification methodology.

To further assess the adaptive AGM's detection ability, we applied the method to selected observational data obtained from the CRISP instrument found on the Swedish 1 m Solar Telescope (Scharmer et al. 2003, 2008). The AGM and Γ methods were applied to the same observational data set, and statistical results were compared to the previously obtained numerical results. It was found that the adaptive AGM extracted more vortices than the Γ method and was more capable of capturing both smaller- and larger-scale vortices.

Both methods obtained comparable vortex sizes: the adaptive AGM, 0.164 Mm^2, versus the Γ method, 0.2 Mm^2. The adaptive AGM found a smaller mean diameter than that calculated by the Γ method, in accordance with the results from numerical data. Also, the adaptive AGM was able to detect both smaller- and larger-scale vortices, as indicated by the tails of the distributions in Figure 14, reproducing similar results to the numerical data. Therefore, the adaptive AGM works for the identification of realistic irregular vortices. The ratio of average lifetimes calculated by both methods was nearly equal to 1; however, compared with the corresponding statistical analysis with the numerical data, we found that the mean lifetime of the detected vortices in the observational data is smaller than that in the numerical data. Moreover, the instantaneous vortex detection rate in the observational data is far less than in the numerical data. The reason behind this is that the resolution of the observational data used for comparison is 12 times smaller than the numerical simulation data resolution and does not involve any limitations of the advanced AGM.

The vortices extracted by the AGM tend to have an oval boundary with a vortex core located near the center of the vortical structure. By analyzing the vortex properties, the mean tangential velocity component is larger than the corresponding radial velocity component, and the magnitude of the tangential velocity component increases when the component is farther from the vortex center. This result is consistent with the previous finding by Silva et al. (2020). By tracking vortices detected by the AGM over a period of time, we found that the size of the vortical structure tends to vary and will shrink as the vortical structure ceases to exist. The vorticity at the center of the vortex is not constant, oscillating as a function of time and steeply decaying close to the end of the vortex lifetime. Therefore, vortices exhibiting a fast vorticity decay are likely to be at the ends of their lives. The velocity components, radial and tangential, also display a distinct radial profile at the beginning and at the end of the life of a vortex. In particular, both components tend to decrease around the vortex center as the vortical structure is decaying. In summary, the developed adaptive AGM is able to precisely capture a number of essential aspects of the vortex geometry and dynamics. Therefore, the proposed automated algorithm can be used to recover crucial information on photospheric vortices and statistical results. In an era of high-resolution observational data—for example, DKIST (Rast et al. 2021), the European Solar Telescope (Quintero Noda et al. 2022), and SULIS (Scullion et al. 2022)—we expect that the proposed algorithm and methodology will provide the necessary accuracy for photospheric vortex detection.

Appendix A
The General Format of the Convolution Kernels

Gonzalez et al. ([2004](#)) have shown that the outer product $a \otimes b$ can be represented as convolution $a \circledast b$ ("padded" convolution operation). The graphical explanation of this is presented in Figures [17](#) and [18](#). Here, a and b are column and

$$PM_x = \begin{bmatrix} -n & \cdots & -2 & -1 & 0 & 1 & 2 & \cdots & n \\ \vdots & & & & \vdots & & & & \vdots \\ -n & \cdots & -2 & -1 & 0 & 1 & 2 & \cdots & n \\ -n & \cdots & -2 & -1 & 0 & 1 & 2 & \cdots & n \\ -n & \cdots & -2 & -1 & 0 & 1 & 2 & \cdots & n \\ -n & \cdots & -2 & -1 & 0 & 1 & 2 & \cdots & n \\ -n & \cdots & -2 & -1 & 0 & 1 & 2 & \cdots & n \\ \vdots & & & & \vdots & & & & \vdots \\ -n & \cdots & -2 & -1 & 0 & 1 & 2 & \cdots & n \end{bmatrix}, PM_y = \begin{bmatrix} -n & \cdots & -n & -n & -n & -n & -n & \cdots & -n \\ \vdots & & & & \vdots & & & & \vdots \\ -2 & \cdots & -2 & -2 & -2 & 1 & 2 & \cdots & -2 \\ -1 & \cdots & -1 & -1 & -1 & 1 & -1 & \cdots & -1 \\ 0 & \cdots & 0 & 0 & 0 & 0 & 0 & \cdots & 0 \\ 1 & \cdots & 1 & 1 & 1 & 1 & 1 & \cdots & 1 \\ 2 & \cdots & 2 & 2 & 2 & 2 & 2 & \cdots & 2 \\ \vdots & & & & \vdots & & & & \vdots \\ n & \cdots & n & n & n & n & n & \cdots & n \end{bmatrix}, \tag{A1}$$

$$\|PM\| = \sqrt{(PM_x).^2 + (PM_y).^2} = \begin{bmatrix} \sqrt{2n^2} & \cdots & \sqrt{n^2+2^2} & \sqrt{n^2+1^2} & n & \sqrt{n^2+1^2} & \sqrt{n^2+2^2} & \cdots & \sqrt{2n^2} \\ \vdots & & & & \vdots & & & & \vdots \\ \sqrt{n^2+2^2} & \cdots & \sqrt{8} & \sqrt{5} & 2 & \sqrt{5} & \sqrt{8} & \cdots & \sqrt{n^2+2^2} \\ \sqrt{n^2+1^2} & \cdots & \sqrt{5} & \sqrt{2} & 1 & \sqrt{2} & \sqrt{5} & \cdots & \sqrt{n^2+1^2} \\ n & \cdots & 2 & 1 & 0 & 1 & 2 & \cdots & n \\ \sqrt{n^2+1^2} & \cdots & \sqrt{5} & \sqrt{2} & 1 & \sqrt{2} & \sqrt{5} & \cdots & \sqrt{n^2+1^2} \\ \sqrt{n^2+2^2} & \cdots & \sqrt{8} & \sqrt{5} & 2 & \sqrt{5} & \sqrt{8} & \cdots & \sqrt{n^2+2^2} \\ \vdots & & & & \vdots & & & & \vdots \\ \sqrt{2n^2} & \cdots & \sqrt{n^2+2^2} & \sqrt{n^2+1^2} & n & \sqrt{n^2+1^2} & \sqrt{n^2+2^2} & \cdots & \sqrt{2n^2} \end{bmatrix}, \tag{A2}$$

where $n \in \mathbb{Z}^+$.

Appendix B
Proof of Separable Convolution Kernel

If $h(m, n)$ is a matrix of size $m \times n$ and its rank is equal to 1, then matrix h can be represented as the outer product of two vectors, $w_1(m, 1)$ and $w_2(1, n)$, as

$$h(m, n) = w_1(m, 1) \otimes w_2(1, n), \tag{B1}$$

where $w_1(m, 1)$ is a column vector of size $m \times 1$ and $w_2(1, n)$ is a row vector of size $1 \times n$.

row vectors of size 5, respectively. Figure [17](#) shows the result of the outer product between a and b; that is, a matrix of 5×5 elements. The convolution procedure is detailed in Figures [18](#)(a)–(d), where the operation performed in this example is referred to as the "padded convolution." The first step of this operation is to rotate the row vector b by 180° and perform multiplication sequentially between the rotated row vector and the first element of the column vector to compute each element in the first row of the output matrix; see Figure [18](#)(a). Then the same procedure is applied between the rotated row vector b and the column vector a's second element (Figure [18](#)(b)) to compute the second row of the output matrix. This procedure continues until the last element of the column vector (Figure [18](#)(c)). Figure [18](#)(d) shows the result of the convolution.
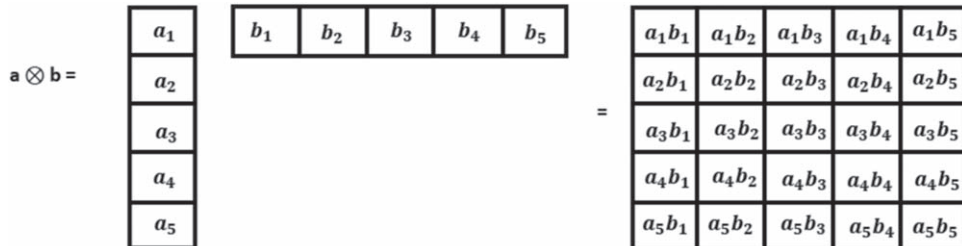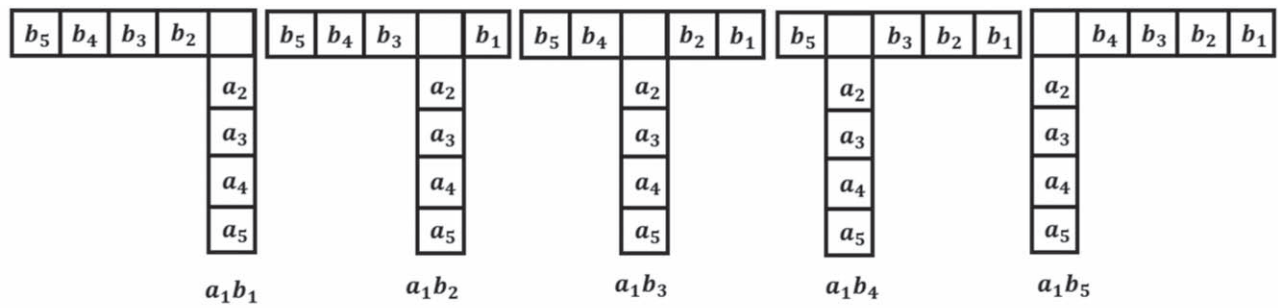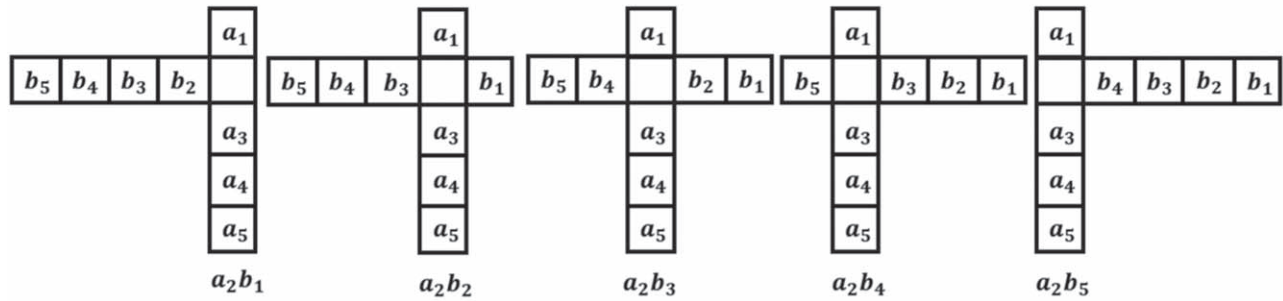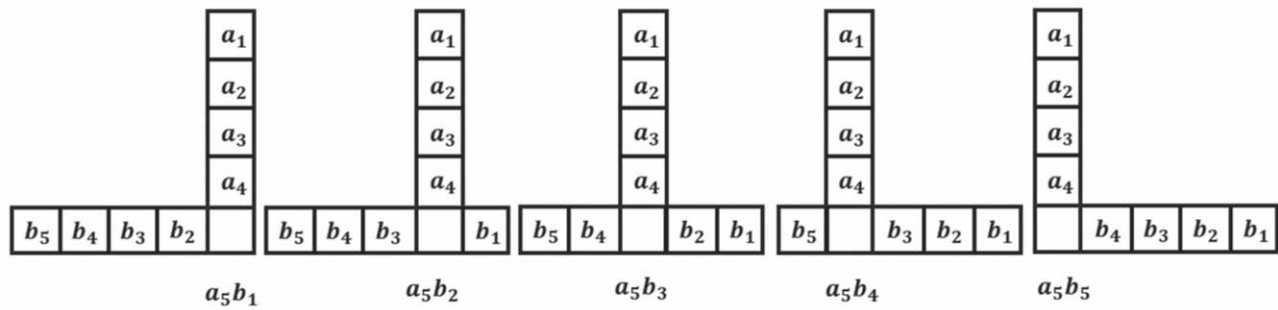

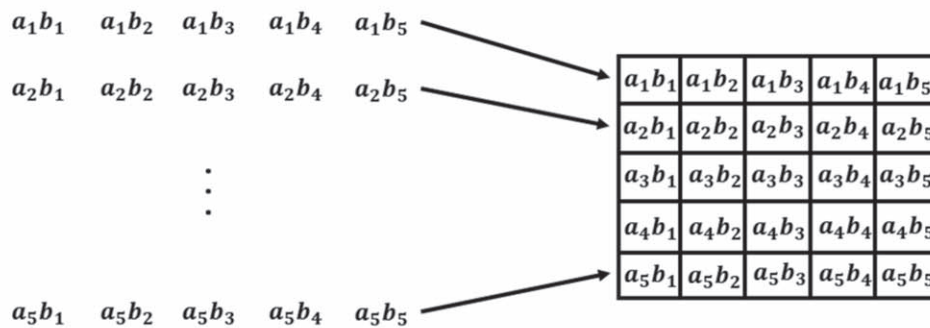**Figure 17.** The outer product between column vector a and row vector b.

Figure 18. Convolution between column vector **a** and row vector **b**. (a) The output of the first row of the convolution between column vector **a** and row vector **b**. (b) The output of the second row of the convolution between column vector **a** and row vector **b**. (c) The output of the fifth row of the convolution between column vector **a** and row vector **b**. (d) The output of the convolution between **a** and **b**.

Appendix C
Computational Cost

When applying the convolution operation between a matrix of size $M \times N$ and a separable convolution kernel of size $m \times n$, the result will require approximately $M \times N \times m \times n$ multiplications and additions without using the kernel's separability. If the separability of the kernel is being applied—that is, the above kernel is being decomposed into a column vector of size $m \times 1$ and a row vector of size $1 \times n$—then the calculation will have two steps. The first step is applying the convolution between the matrix and the column vector, and the corresponding multiplications and additions are about $M \times N \times m$. The second step will perform the convolution between the output result of the first step (the output size of the first step remains $M \times N$) and the row vector. The second step will have $M \times N \times n$ multiplications and additions. Thus, the total multiplications and additions of the calculation when applying the kernel's separability will be $MN(m + n)$. When $m = n$, the

convolution kernel is square. By comparing the computational complexity between the direct and the separable convolution, the estimated computational advantage is

$$\frac{MNmn}{MN(m + n)} = \frac{mn}{(m + n)} = \frac{m}{2}. \tag{C1}$$

This ratio means that the AGM Γ_1 is expected to be $\frac{m}{2}$ times faster than the CGM Γ_1 in each convolution operation between the velocity domain and each separable kernel.

Appendix D
Unnormalized AGM versus CGM

Figure 19 shows the detection result when using $ks = 33$. Figure 20 displays the corresponding distributions of ratios (i.e., C_1 and C_2) between the unnormalized AGM and CGM for Γ_1 and Γ_2 when using $ks = 33$.
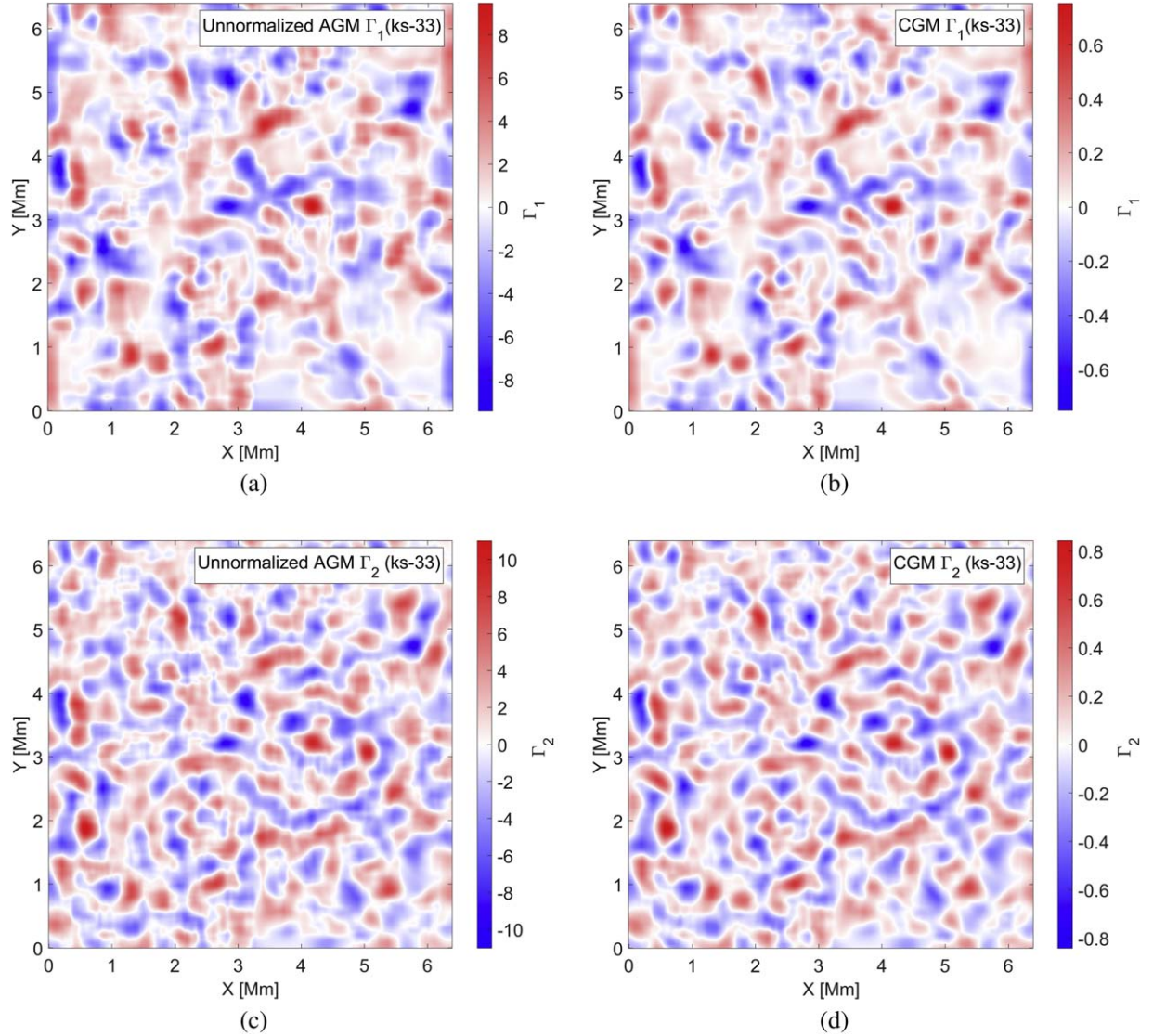

Figure 19. The distributions of the Γ function values obtained by the AGM ((a) and (c)) and CGM ((b) and (d)) that were applied to the photospheric horizontal velocity field are shown in Figure 1. For both cases, a convolution kernel size $ks = 33$ was applied. As here, the values of Z_1 and Z_2 for the AGM were equal to 1 and the AGM was unnormalized.
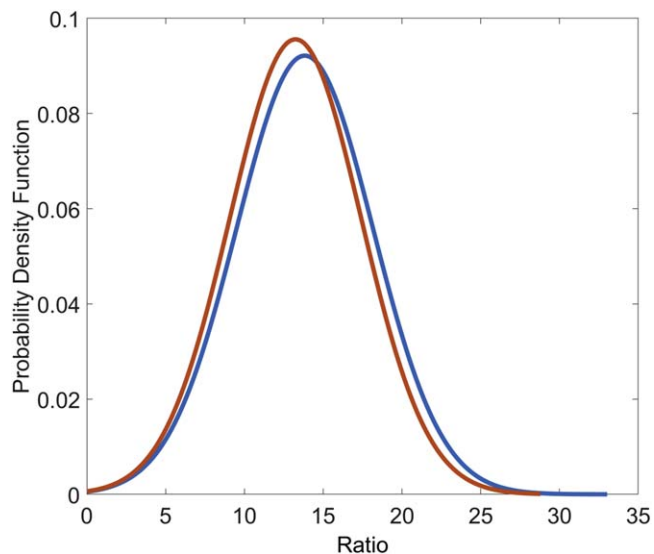
Figure 20. The distribution of the ratios between the unnormalized AGM (Figures 19(a) and (c)) and CGM (Figures 19(b) and (d)) for Γ_1 (C_1 is shown in blue) and Γ_2 (C_2 is shown in red). For both cases, the convolution kernel is equal to 33.

ORCID iDs

Yuyang Yuan ⬤ https://orcid.org/0000-0002-0754-9149
Suzana de Souza e Almeida Silva ⬤ https://orcid.org/0000-0001-5414-0197
Viktor Fedun ⬤ https://orcid.org/0000-0002-0893-7346
Irina N. Kitiashvili ⬤ https://orcid.org/0000-0003-4144-2270
Gary Verth ⬤ https://orcid.org/0000-0002-9546-2368

References

Aljohani, Y., Fedun, V., Ballai, I., et al. 2022, ApJ, 928, 3
Attie, R., Innes, D. E., & Potts, H. E. 2009, A&A, 493, L13
Balmaceda, L., Vargas Domínguez, S., Palacios, J., Cabello, I., & Domingo, V. 2010, A&A, 513, L6
Bonet, J. A., Márquez, I., Sánchez Almeida, J., et al. 2010, ApJL, 723, L139
Bonet, J. A., Márquez, I., Sánchez Almeida, J., Cabello, I., & Domingo, V. 2008, ApJL, 687, L131
Brandt, P. N., Scharmer, G. B., Ferguson, S., et al. 1988, Natur, 335, 238
Canivete Cuissa, J. R., & Steiner, O. 2020, A&A, 639, A118
Chian, A. C. L., Silva, S. S. A., Rempel, E. L., et al. 2019, MNRAS, 488, 3076
Chian, A. C. L., Silva, S. S. A., Rempel, E. L., et al. 2020, PhRvE, 102, 060201
Dakanalis, I., Tsiropoula, G., Tziotziou, K., & Kontogiannis, I. 2022, A&A, 663, A94
Dakanalis, I., Tsiropoula, G., Tziotziou, K., & Koutroumbas, K. 2021, SoPh, 296, 17
Fedun, V., Shelyag, S., Verth, G., Mathioudakis, M., & Erdélyi, R. 2011, AnGeo, 29, 1029
Giagkiozis, I., Fedun, V., Scullion, E., Jess, D. B., & Verth, G. 2018, ApJ, 869, 169
Gonzalez, R. C., Woods, R. E., & Eddins, S. L. 2004, Digital Image Processing Using Matlab™ (3rd ed.; Knoxville, TN: Gatesmark Publishing)
Graftieaux, L., Michard, M., & Grosjean, N. 2001, MeScT, 12, 1422
Günther, T., & Theisel, H. 2018, Comput. Graph. Forum, 37, 149
Haller, G., Hadjighasem, A., Farazmand, M., & Huhn, F. 2016, JFM, 795, 136
Iijima, H., & Yokoyama, T. 2017, ApJ, 848, 38
Kato, Y., & Wedemeyer, S. 2017, A&A, 601, A135
Kitiashvili, I. N., Abramenko, V. I., Goode, P. R., et al. 2012, arXiv:1206.5300
Kitiashvili, I. N., Kosovichev, A. G., Lele, S. K., Mansour, N. N., & Wray, A. A. 2013, ApJ, 770, 37
Kitiashvili, I. N., Kosovichev, A. G., Mansour, N. N., & Wray, A. A. 2011, ApJL, 727, L50
Moll, R., Cameron, R. H., & Schüssler, M. 2011, A&A, 533, A126
Nordlund, A. 1985, SoPh, 100, 209
Nordlund, Å., Stein, R. F., & Asplund, M. 2009, LRSP, 6, 2
Quintero Noda, C., Schlichenmaier, R., Bellot Rubio, L. R., et al. 2022, A&A, 666, A21
Rast, M. P., Bello González, N., Bellot Rubio, L., et al. 2021, SoPh, 296, 70
Requerey, I. S., Cobo, B. R., Gošić, M., & Bellot Rubio, L. R. 2018, A&A, 610, A84
Scharmer, G. B. 2006, A&A, 447, 1111
Scharmer, G. B., Bjelksjo, K., Korhonen, T. K., Lindberg, B., & Petterson, B. 2003, Proc. SPIE, 4853, 341
Scharmer, G. B., Narayan, G., Hillberg, T., et al. 2008, ApJL, 689, L69
Schuessler, M. 1984, A&A, 140, 453
Scullion, E., Morgan, H., Lin, H., Fedun, V., & Morton, R. 2022, ExA, 54, 317
Shelyag, S., Fedun, V., Erdélyi, R., Keenan, F. P., & Mathioudakis, M. 2012, in ASP Conf. Ser. 463, Second ATST-EAST Meeting: Magnetic Fields from the Photosphere to the Corona, ed. T. R. Rimmele et al. (San Francisco, CA: ASP), 107
Silva, S. S. A., Fedun, V., Verth, G., Rempel, E. L., & Shelyag, S. 2020, ApJ, 898, 137
Silva, S. S. A., Rempel, E. L., Pinheiro Gomes, T. F., Requerey, I. S., & Chian, A. C. L. 2018, ApJL, 863, L2
Silva, S. S. A., Verth, G., Rempel, E. L., et al. 2021, ApJ, 915, 24
Skirvin, S., Verth, G., Juan González-Avilés, J., et al. 2023, AdSpR, 71, 1866
Snow, B., Fedun, V., Gent, F. A., Verth, G., & Erdélyi, R. 2018, ApJ, 857, 125
Tziotziou, K., Scullion, E., Shelyag, S., et al. 2023, SSRv, 219, 1
Wedemeyer-Böhm, S., Scullion, E., Steiner, O., et al. 2012, Natur, 486, 505
Wray, A. A., Bensassi, K., Kitiashvili, I. N., Mansour, N. N., & Kosovichev, A. G. 2015, arXiv:1507.07999
Yadav, N., Cameron, R. H., & Solanki, S. K. 2020, ApJL, 894, L17
Yadav, N., Cameron, R. H., & Solanki, S. K. 2021, A&A, 645, A3
Yadav, N., Keppens, R., & Popescu Braileanu, B. 2022, A&A, 660, A21
Zhou, J., Adrian, R. J., Balachandar, S., & Kendall, T. M. 1999, JFM, 387, 353
Zigunov, F., Sellappan, P., & Alvi, F. S. 2020, in AIAA Scitech 2020 Forum (Reston, VA: American Institute of Aeronautics and Astronautics), AIAA 2020–1322